



Diurnal cycles of cloud cover and its vertical distribution over the Tibetan Plateau revealed by satellite observations, reanalysis datasets and CMIP6 outputs

Yuxin Zhao¹, Jiming Li^{1*}, Lijie Zhang¹, Cong Deng¹, Yarong Li¹, Bida Jian¹, Jianping Huang¹

5 ¹Key Laboratory for Semi-Arid Climate Change of the Ministry of Education, College of Atmospheric Sciences, Lanzhou University, Lanzhou, China

Correspondence to: Jiming Li (lijiming@lzu.edu.cn)

Abstract. Diurnal variations of cloud cover and cloud vertical distribution are of great importance to earth-atmosphere system radiative budgets and climate change. However, thus far, these topics have received insufficient attention, especially on the Tibetan Plateau (TP). This study focuses on the diurnal variations of total cloud cover, cloud vertical distribution, and cirrus clouds and their relationship to meteorological factors over the TP based on active and passive satellite observations, reanalysis data, and CMIP6 outputs. Our results are consistent with previous studies but provide new insights. The results show that total cloud cover peaks in the afternoon, especially over the southeastern TP, but the spatial and temporal distributions of clouds from different datasets are inconsistent. To some extent, it could be attributed to subvisible clouds missed by passive satellites and models. Compared with satellite observations, the amplitudes of the diurnal variations of total cloud cover obtained by the reanalysis and CMIP6 models are obviously smaller. The CATS can capture varying pattern of the vertical distribution of clouds and corresponding height of peak cloud cover at middle and high atmosphere levels, although it underestimates the cloud cover of low-level clouds especially over the southern TP. Compared with CATS, ERA5 cannot capture the complete diurnal variations of vertical distribution of clouds and the MERRA-2 has a poorer performance. We further find that cirrus clouds, which are widespread over the TP, show significant diurnal cycle and spatial and temporal distribution characteristics, with peak cloud cover over 0.4 during 15:00-21:00 LT over the northeastern TP. Be different from tropic, where thin cirrus ($0.03 < \text{optical depth} < 0.3$) dominate, opaque cirrus clouds ($0.3 < \text{optical depth} < 3$) are the dominant cirrus clouds over the TP. The cloud cover of opaque cirrus reaches a daily maximum of ~ 0.24 over the northeastern TP at 15:00 LT, and are influenced by diurnal variations of the 2-m temperature and 250 hPa vertical velocity. Although subvisible clouds ($\text{optical depth} < 0.03$), which have a potential impact on the radiation budget, are the fewest among cirrus clouds over the TP, the cloud cover can reach 0.1 during 21:00-03:00 LT, and their diurnal cycle is obviously consistent with that of the high-level relative humidity. Our results will help reduce uncertainties in simulations of diurnal variations of cloud cover in models and reanalysis data over the TP region.

1 Introduction

30 The Tibetan Plateau (TP), a heat source for the East Asian monsoon, has received worldwide attention due to its prominent altitude and special topography (Wu et al., 2017). Over the TP, surface heating causes a low-pressure centre that



can attract warm-moist air convergence from the ocean and then promote convection activities (Wu et al., 2012). The abundant water storage in the atmosphere over the TP and its surrounding regions can be explained by this convective system, and the TP is thus called the “Asian water tower” (Xu et al., 2008). In recent decades, the TP has experienced significant climate warming (Yao et al., 2012; Liu and Chen, 2000), and it will continue in the future (Duan and Wu, 2006; Wang et al., 2008). The rapid warming over the TP has caused dramatic changes in the cryosphere, such as glacier retreat, snow cover reduction, permafrost degradation and expansion of glacier-fed lake areas (Zhang et al., 2019; Rangwala et al., 2010; Yao et al., 2007; Cheng and Wu, 2007). Although some studies have found that rapid warming is possibly linked to increasing surface water vapour or anthropogenic greenhouse gas emissions over the TP (Rangwala et al., 2009; Zhou and Zhang, 2021), growing evidence has verified that variations in cloud properties are also very important in determining the surface energy balance and water cycle of the TP region (Pan et al., 2017; Yang et al., 2012; Yan et al., 2016).

Indeed, cloud cover is the first-order variable impacting downwelling radiation at the surface (Naud et al., 2015), and its long-term changes over the TP and consequential influences have been explored based on satellite observations and reanalysis data (You et al., 2014; Kukulies et al., 2019). For example, based on weather observations at stations across the TP during 1961–2003, Duan and Wu (2006) found a dramatic increase in the low-level cloud amount, which ultimately led to strong nocturnal surface warming. Ma et al. (2021) also point out that high cloud cover is the most important influence factor on summer precipitation over the TP, based on the Clouds and Earth's Radiant Energy System (CERES) Edition 4 dataset during 2001–2009. In addition to the long-term change, however, existing studies indicate that clouds over the TP also exhibit obvious diurnal cycles. The observations from ground-based cloud radar at the Motuo National Climate Observatory over the southeastern TP show that the occurrence frequency of clouds is larger (maximum value 73%) from evening to midnight (i.e., 13:00–18:00 UTC) and reaches a minimum value (53%) in the morning (04:00 UTC) (Zhou et al., 2021). The diurnal cycle of clouds strongly affects their efficiency in regulating the radiation budget (Yin and Porporato, 2020), and it is also closely related to the diurnal cycle of precipitation (Zhao et al., 2017; Nesbitt et al., 2008). Neglecting the importance of the diurnal cycle of clouds will result in the inaccurate representation of clouds in models and exacerbate inconsistencies between observations and model simulations (Tian et al., 2004). For example, the evaluation of version 2 of the Community Climate System Model (CCSM2) shows that the simulated diurnal variations are still smaller than the observed values even if the model is driven by observational data, and the diurnal cycle of precipitation from simulations is too weak over the oceans (Dai and Trenberth, 2004). Yin and Porporato (2017) found that most General Circulation Models (GCMs) lack cloud peaks around the afternoon and thus lead to the overestimation of daily mean top-of-atmosphere (TOA) irradiance compared with ERA-20C. Moreover, the inconsistent amplitudes and phases of the diurnal cycle of the clouds between models results in a large intermodel difference in irradiance, which reaches a maximum of 1.8 Wm^{-2} over land and 2.1 Wm^{-2} over the ocean. To date, some observational studies have focused on diurnal variations of cloud cover over the TP based on geostationary satellite data and ground-based observations (Shang et al., 2018; Liu et al., 2015), and some typical features of the diurnal cloud cycle have been described, e.g., amplitude and phase (Song et al., 2017). However, satellites with passive remote sensing instruments (e.g., MODIS) generally fail to detect optically thin clouds with small optical depths



(<0.3) (Minnis et al., 2008), which are found in approximately 50% of global observations (Sun et al., 2011a). These thin cirrus clouds frequently occur near the tropopause of stronger convective regions (e.g., the tropics or the Tibetan Plateau) and have great impacts on the cloud or surface properties retrieved by satellite, Earth–atmosphere system radiation energy budgets, and exchanges between the troposphere and stratosphere (Sassen and Benson, 2001; Sun et al., 2011a; Zou et al., 2020; Sun et al., 2011b). In addition, the thin cirrus clouds that are undetected by passive sensors also possibly contribute to part of the total cloud cover inconsistency between passive and active satellites (Stanfield et al., 2015). It is therefore of fundamental importance to study these optically thin clouds over the TP in detail, especially the relationship between their diurnal cycle and meteorological factors, to fill in related knowledge gaps in the TP region.

In addition, another important but less concerning issue in the TP region is the cloud vertical distribution, especially its diurnal cycle. The vertical profile of the cloud cover may affect the atmospheric circulation by altering the vertical gradients of the radiative heating/cooling rate and the subsequent atmospheric temperature and is also closely linked to the efficiency of precipitation production (Posselt et al., 2008; Binder et al., 2020). To date, however, too few studies have focused on the diurnal cycle of cloud vertical distribution over the TP because passive sensors onboard geostationary satellites cannot resolve the vertical structure of cloud systems. The Cloud–Aerosol Lidar and Infrared Pathfinder Satellite Observation (CALIPSO) and CloudSat satellites have a vertically resolved ability to detect the cloud vertical structure at a global scale (Oreopoulos et al., 2017; Sassen et al., 2009). Although CALIPSO/CloudSat provide considerable valuable information on cloud vertical distribution, especially over areas sensitive to climate change without ground-based observations (Wang et al., 2021; Yan et al., 2016), only instantaneous cloud vertical distributions at two overpass times are possible. As a result, this study attempts to use the measurements from the Cloud-Aerosol Transport System (CATS) (Mcgill et al., 2015) lidar onboard the International Space Station (ISS), which has similar advantages as the Cloud-Aerosol Lidar with Orthogonal Polarization (CALIOP) onboard the CALIPSO for detecting optically thin clouds and cloud vertical distribution (Yorks et al., 2016), to analyse the diurnal cycle of total cloud cover, vertical distribution and optically thin cirrus clouds over the TP. The CATS is the only space-based lidar that contains active vertical measurements with a variable local time of overpass between 51°S and 51°N and shows sufficient credibility compared to ground-based active instruments and passive and active spaceborne sensors (Noel et al., 2018). This makes it possible for the CATS to analyse the diurnal cycle of cloud vertical distribution at regional or near-global scales (Dauhut et al., 2020; Wang et al., 2022). In addition to the CATS, this study employs cloud cover from other datasets, such as passive satellite (Himawari-8, ISCCP), reanalysis datasets (ERA5, MERRA-2) and climate model (CMIP6) outputs, to perform related comparisons. The paper is organized as follows. The data and methods used in this study are described in Section 2. Section 3 includes the comparison of diurnal variations of total cloud cover and cloud vertical structure between different datasets. The correlation between the diurnal cycle of cirrus and meteorological factors is further discussed. Finally, the conclusions and discussion are presented in Section 4.



2 Data and methods

Due to sparse ground-based measurements over the TP, this investigation mainly uses multiple satellite products, reanalysis datasets and outputs of CMIP6 models to analyse the diurnal cycle of the cloud cover over the TP region (26–40° N and 73°–105° E). In addition, the TP is simply divided into four subregions by the latitude and longitude lines of 33° N and 89° E, respectively, and the boundary of the TP (Xiaoduo et al., 2019).

2.1 Cloud-Aerosol Transport System (CATS)

The CATS lidar onboard the ISS is a multiwavelength elastic backscatter lidar that can measure backscattered energy profiles with nearly a three-day repeating cycle over the same locations but at different local times between 51°S and 51°N (McGill et al., 2015). Although the CATS cannot monitor the evolution of one cloud system, its special sample mode makes it the only space-based lidar by far that provides the seasonal-averaged diurnal cycle of clouds and their aerosol properties, especially their vertical profiles, at a given location by aggregating observations at different local times of day during various seasons (Noel et al., 2018). The CATS employs a similar atmospheric layer-detection algorithm as the CALIOP to clarify the cloud/aerosol layer and retrieve its properties (Yorks et al., 2016), but unlike the CALIOP, the CATS uses the attenuated backscatter at 1064 nm instead of 532 nm because the signals at 532 nm are unavailable due to technical issues (Yorks et al., 2016). In addition, the signal-to-noise ratio at 1064 nm is higher at nighttime (Pauly et al., 2019), and the absorbing aerosol layer is more fully captured by 1064 nm (Rajapakshe et al., 2017; Yorks et al., 2021). Recently, some studies have confirmed the good performance of the CATS in retrieving cloud/aerosol property profiles, especially the diurnal variations, for scientific investigations (Noel et al., 2018; Yu et al., 2021).

In this investigation, we use the related cloud layer parameters from Version 3-01 of the CATS level 2 operational (L2O), 5 km layer product (L20_D/N-M7.2-V3-01_5kmLay) during the entire period of the CATS rotation (March 2015–October 2017), including the ‘Feature Type Score’, ‘Layer Base Altitude’, ‘Layer Top Altitude’, ‘Layer Top Temperature’ and ‘Feature Optical Depth’. Here, we use cloudy profiles with a ‘Feature Type Score’ of 5 or greater to reduce the uncertainty of the layer-detection algorithm (Yorks et al., 2016; Noel et al., 2018). In addition, for a given grid (e.g., 2° × 2°), the total cloud cover based on the CATS is calculated by dividing the number of cloudy profiles by the total number of profiles in each grid (Li et al., 2011; Noel et al., 2018). The cloud cover at a given height bin has a similar definition as the total cloud cover.

2.2 International Satellite Cloud Climatology Project (ISCCP)

The ISCCP dataset (Rossow and Schiffer, 1999), which is obtained from both geostationary and polar-orbiting satellite imaging radiometers with common visible and infrared channels, has been widely used to study the diurnal, seasonal and interannual variations in cloud properties (Naud and Chen, 2010; Norris and Evan, 2015; Rossow et al., 2021). Compared with the previous version of the ISCCP dataset (e.g., ISCCP-D), the newly released ISCCP-H product has many



improvements (Young et al., 2018), such as a finer sampling resolution, higher data quality and expanded record period. To date, the ISCCP-H product can provide the global total cloud cover with a $1^\circ \times 1^\circ$ spatial resolution every 3 hours from July 130 1983 through June 2017, and it has also been used in some recent studies to analyse the diurnal cycle and long-term variation in regional cloud cover (Zhang et al., 2020b; Lei et al., 2020), in model evaluation (Tselioudis et al., 2021), and in comparison with other satellite cloud products (Karlsson and Devasthale, 2018; Tzallas et al., 2019). In this investigation, we use the “cloud area fraction” parameter from the 3-hourly monthly averaged ‘ISCCP Basic HGH’ dataset from March 2015 to June 2017.

135 2.3 Himawari-8 geostationary satellite

The Himawari-8 geostationary satellite was launched by the Japan Meteorological Agency on 7 October 2014. The Advanced Himawari Imager (AHI), which is carried by Himawari-8, has 16 bands, including 3 visible bands, 3 near-infrared bands, and 10 other infrared channels. Based on the radiance information of these channels, the AHI can provide good-quality cloud and aerosol products with a spatial resolution from 0.5 to 2 km and a temporal resolution from 2.5 to 10 min 140 (Letu et al., 2020; Letu et al., 2018). Here, the “Cloud Mask Confidence Level Flag” parameter in the Level-2 (L2) operational cloud property products from January 2016 to October 2017 is used in the following analysis. The “Cloud Mask Confidence Level Flag” provided by the Himawari-8 classifies each 0.05° grid into the following four categories: clear, probably clear, probably cloudy, and cloudy. Similar to previous studies (Shang et al., 2018; Lei et al., 2020), only the ‘cloudy’ pixels are identified as clouds, while the others are classified as clear sky in this study. Finally, the total cloud cover 145 given at each 0.05° grid is defined as the ratio of the cloudy sample size to the total sample size every 3 hours. In addition, because the detection range of the AHI moves daily, we consider only the period in which there are complete data over the TP, which is during 6:00 LT (local time) to 16:00 LT.

2.4 Reanalysis datasets

The ERA5 reanalysis dataset from the European Centre for Medium-Range Weather Forecast (ECMWF) contains 150 abundant variables at the surface and on single levels and pressure levels by using 4D-Var data assimilation and model forecasts of the ECMWF Integrated Forecast Systems (IFS) (Hersbach et al., 2020; Urraca et al., 2018). Unlike satellite observations of cloud cover, cloud characteristics from reanalysis data largely depend on atmospheric numerical models and data assimilation schemes. The physical parameterizations in ERA5 that provide the cloud properties in a grid cell are based on the advanced version of the scheme by Tiedtke (1993). In this study, the hourly total cloud cover for a single level and 155 fraction of cloud cover for each pressure level from ERA5 at a $0.25^\circ \times 0.25^\circ$ resolution are used to compare the diurnal cycle of the cloud cover and its vertical distribution with other datasets. In addition, the hourly 2-m temperature, 10-m wind speed, vertically integrated divergence of moisture flux on single levels and hourly vertical velocity and relative humidity at 250 hPa on the pressure levels are used to discuss the relation between the cloud cover and meteorological parameters.



In addition to the ERA5, the cloud cover from version 2 of the Modern-Era Retrospective Analysis for Research and
160 Applications (MERRA-2) (Rienecker et al., 2011), which has a gridded resolution of $0.5^\circ \times 0.625^\circ$, is also used. MERRA-2
is the latest atmospheric reanalysis produced by NASA's Global Modeling and Assimilation Office (GMAO). The Goddard
Earth Observing System (GEOS) atmospheric model (Rienecker, 2008; Molod et al., 2015) and NCEP's grid point statistical
interpolation (GSI) analysis scheme (Wu et al., 2002; Kleist et al., 2009) are the key components of version 5.12.4 of the
165 GEOS atmospheric data assimilation system that produce MERRA-2. Specifically, this study uses the hourly total cloud area
fraction from the MERRA-2 'tavgl_2d_rad_Nx' product, which is a time-averaged 2-dimensional dataset. The cloud cover
for radiation at 42 pressure levels is based on the MERRA-2 'tavg3_3d_rad_Np' product, which is a 3-dimensional 3-hourly
time-averaged dataset.

2.5 CMIP6 models

Here, we also use the 3-hourly cloud area fraction from 12 CMIP6 models with AMIP simulations that utilize observed
170 sea surface temperatures and sea ice concentrations (Eyring et al., 2016). Assessment of the CMIP6's performance with
respect to clouds is of wide concern and has achieved variable results (Cherian and Quaas, 2020; Vignesh et al., 2020).
Because the temporal coverage of the historical CMIP6 outputs cannot cover the same detection period as the CATS, we use
the AMIP simulations from January 1979 to December 2014. In addition, it is worth noting that CMIP6 simulations of the
satellite data involved in this study are unavailable for the 3-hourly cloud area fraction. Due to the discrepancies in the
175 definitions and determination algorithms of cloud cover, direct comparisons between the diurnal cycle of total cloud cover in
models and satellite observations possibly results in some uncertainties (Engström et al., 2015). Table 1 lists the details of
the satellite products, reanalysis datasets and model outputs in this study, including their spatial-temporal resolutions and
temporal coverage.

3 Results

180 3.1 Comparison of the diurnal variation in total cloud cover from different datasets

The diurnal cycle of cloud properties over the TP shows unique characteristics due to its special topography and large-
scale circulation background (Wang et al., 2020). Fig. 1 shows the spatial distribution of total cloud cover over the TP for
each 3-hour mean using active and passive satellite datasets, reanalysis data and climate model outputs. Similar to previous
studies (Lei et al., 2020; Shang et al., 2018), significant diurnal variations of total cloud cover over the TP are found in
185 almost all datasets. The peak time and amplitude of total cloud cover both exhibit obvious differences among the different
datasets due to difference in the sensitivities of detectors, cloud detecting algorithms or cloud parameterizations. For the
CATS, clouds have a maximum coverage in the early afternoon (e.g., 12:00 LT), especially the total cloud cover during this
time, which reaches a daily maximum of 0.8 over the central and eastern TP. However, a daily minimum total cloud cover
(mean value <0.5) over the southwestern TP is found at 06:00 LT. The diurnal variations of total cloud cover from the



190 ISCCP are similar to those of the CATS except that a smaller total cloud cover from the ISCCP occurs in the southeastern part of the TP at night (e.g., 21:00 LT, 00:00 LT). Compared with the ISCCP, the higher total cloud cover over the eastern TP (especially at night) detected by the CATS might be related to the optically thin cirrus clouds (also see Fig. S3c), which are usually misclassified as clear sky by passive sensors or satellites such as those of the ISCCP, MODIS, and MISR because their minimum detectable cloud optical thickness is approximately 0.1 to 0.4 (Marchand et al., 2010). Indeed, by comparing
195 the total cloud cover from the Aqua/MODIS and CALIOP, Holz et al. (2008) found that the cloud detection results from the MODIS and CALIOP agreed more than 87% of the time, and their discrepancies were largely associated with the optically thin clouds that were undetected by MODIS but that were readily observed by CALIOP. From a global mean perspective, the optically thin clouds resulting in the total cloud cover from CALIPSO–CloudSat are approximately 10% higher than those from the CERES–MODIS (Stanfield et al., 2015). Sun et al. (2011a) also point out that if these optically thin clouds
200 were completely mistaken for clear sky, approximately 15 Wm^{-2} of the heating effect would be missed. The total cloud cover detected by the Himawari-8 satellite is nearly half that of the CATS, except at 15:00 LT, and our study area is out of scanning after 16:00 LT. This difference may be partly related to the detection limitation of the Himawari-8 and its strict cloud identification algorithm (Imai and Yoshida, 2016). For the higher spatial resolution Himawari-8 and ERA5 data, the total cloud cover shows a higher value on south-facing slopes, likely caused by the small cumulus growth (Shang et al.,
205 2018). However, this phenomenon is not obvious in other datasets, probably because of the difference in resolution. For reanalysis, the daily amplitude of the total cloud cover of the ERA5 is significantly smaller, and the total cloud cover of the MERRA-2 is lower than the results of the CATS most of the time. Similar to the other datasets, the total cloud cover is larger at the eastern and northern TP at 15:00 LT in the MERRA-2, but the high value area moves to the northwestern TP in the ERA5. In addition, we find that the total cloud cover in the ERA5 over the southeastern part of the TP is obviously higher
210 than those from other datasets before dawn (e.g., 03:00 LT and 06:00 LT). This is because the ERA5 overestimates low-level clouds, which will be explained in more detail in Section 3.2, which discusses the vertical distribution of clouds. Generally, the ERA5 underestimates the total cloud cover during daytime compared with the CATS and ISCCP, especially in the afternoon. The total cloud cover in the MERRA-2 is lowest among these datasets and does not exceed 0.7 on any day. From a global perspective, Li et al. (2017) indicate that the MERRA-2 underestimates total cloud cover nearly everywhere
215 compared with the CERES–MODIS dataset, except for in the Intertropical Convergence Zone (ITCZ). The mean total cloud cover of the multimodel CMIP6 (hereafter MEM) is similar to that of the MERRA-2, except that the total cloud cover is slightly larger over the southern TP. The results show that the amplitude of the climate model simulations differs significantly from the satellite results over the TP. This problem exists on a global scale and induces overestimation of radiation in most climate models (Yin and Porporato, 2017). Of course, the comparison of different datasets may be biased
220 due to different time periods (shown in Table 1) and discrepancies in the definitions and determination algorithms of cloud cover, and it may also be limited by the fact that the effective detection periods of each dataset cannot be overlapped. However, after averaging the data over several years, the diurnal variations can be compared to some extent.



Due to the different distributions of temperature, moisture, etc., Fig. 1 clearly shows that the distributions of total cloud cover also exhibit obvious spatial variability at different local times. Here, the TP is simply divided into four subregions
225 along the latitude and longitude lines of 33° N and 89° E (shown in total cloud cover from CATS at 06:00 LT in Fig. 1),
respectively, and diurnal variations of regional averaged total cloud cover over these subregions are provided in Fig. 2. It is
worth noting that this is only a simple and rough zoning method without a detailed matching of dynamic and circulation
structures, which could have an impact on the results, but it can also reflect the differences between the monsoon-controlled
area and the non-monsoon area on the TP to some extent (Yao et al., 2013). Among the different regions of the TP, the total
230 cloud cover over the southwestern TP is the lowest in all the datasets, possibly limited by the moisture flux and the high
terrain of the Himalayas. Over the northwestern TP (Fig. 2a), the range of the diurnal total cloud cover detected by the CATS
is approximately 0.5-0.7, and the peak is approximately 0.7 at 12:00 LT. Compared with the CATS, the ISCCP exhibits a
higher total cloud cover during the daytime and a later peak time at approximately 15:00 LT (maximum value >0.85). After
19:00-20:00 LT, the total cloud cover in the ISCCP is obviously less than that in the CATS, and its minimum value and daily
235 range are approximately 0.5 and 0.35, respectively. The MERRA-2 and MEM have similar diurnal cycles and magnitudes of
total cloud cover, and their peak and valley values (or times) are approximately 0.55-0.6 (16:00 LT) and 0.45-0.5 (09:00 LT),
respectively. The weakest diurnal cycle of the total cloud cover can be found in the ERA5 regardless of subregion, and the
daily range of total cloud cover from the ERA5 is even less than 0.02. In our study, the Himawari-8, which can detect the
total cloud cover of the TP only between 06:00 LT and 16:00 LT, shows a more significant daily range of total cloud cover
240 (>0.4) and is approximately twice as large as that of the CATS. The diurnal cycle of total cloud cover over the southwestern
TP from different datasets is similar to that over the northwestern TP (Fig. 2b). Over the eastern TP, the daily range of total
cloud cover is smaller in most datasets than that over the western TP, especially over the southeastern TP (Fig. 2d). From
Figs. 1 and 2, it is clear that significant total cloud cover differences between different datasets are not only for geophysical
distributions but also for regional means. As stated in Section 2, the total cloud cover differences in satellite datasets partly
245 refer to the detection limitations of different sensors. By comparing the total cloud cover estimated from the CloudSat-
CALIPSO with the ISCCP, Naud and Chen (2010) point out that the total cloud cover from the ISCCP is underestimated by
approximately 18% over the TP, in part due to the misdetection of low-level clouds at night, which can partly explain the
difference between the ISCCP and the CATS at night in our study. However, optically thin clouds are also important
contributors to large differences in cloud cover between the ISCCP and the CATS, especially during summer, when high-
250 level, optically thin clouds occur more often than in the other seasons (Naud and Chen, 2010). Naud and Chen (2010) also
point out that cloud property retrieval from the ISCCP is more consistent with those from the CloudSat-CALIPSO over high-
elevation regions of the TP where multi-layered cloud systems are infrequent. In fact, when the optically thin clouds overlap
with other cloud types, the passive satellite will bias the cloud top properties of the underlying clouds (e.g., cloud top
temperature or height), but the total cloud cover is almost unaffected. However, if only optically thin clouds are present, the
255 ISCCP easily misclassifies them as clear sky. Thus, multi-layered cloud systems are not the main contributors to the total
cloud cover differences between the ISCCP and the CATS. In our study, we also find that larger differences exist between



the ISCCP (or the ERA5) and the Himawari-8, especially at 09:00 LT. Using similar datasets, Lei et al. (2020) show that the ERA5 overestimates approximately 10% and the ISCCP overestimates 20% of the total cloud cover over the TP compared to the Himawari-8. In summary, total cloud cover from multiple sources exhibits considerable regional differences in the phase and magnitude of the diurnal cycle.

To further quantify the spatial consistency of total cloud cover from passive satellites, reanalyses and models with CATS observations at different local times, the Taylor diagram (Taylor, 2001) is used to provide the standard deviation and centred root-mean-square deviation (RMSD, purple circle) normalized by the observed values and the spatial correlation coefficients between other datasets and CATS observations (Fig. 3). Here, all datasets are uniformly interpolated into 0.5° by 0.5° . The standard deviation and RMSD show the changes in amplitudes and phases of the different datasets, respectively. That is, the closer the standard deviation shown by the points in Fig. 4 is to the red line, the closer the amplitude of the spatial difference of the total cloud cover of the datasets and CATS. The smaller the RMSD is, the more similar the distribution pattern is to that of the CATS. The results show that the spatial consistency between some CMIP6 models and the CATS is poor. The correlation coefficient between the FGOALS-f3, FGOALS-g3, IPSL-CM6A-LR and the CATS is even negative at 06:00 LT (Fig. 3a). The mean absolute error (MAE) (shown in Fig. S1) between the MRI-ESM2-0 and the CATS is relatively large, which indicates a large spatial distribution difference, especially at 12:00 LT. Nevertheless, most of the CMIP6 models have a strong correlation with the CATS; in particular, the correlation coefficient between the EC-Earth3 and EC-Earth3-Veg and the CATS is over 0.7 at 12:00 LT and 00:00 LT. The correlation coefficient of the MEM is over 0.5 during most times and approximately reaches 0.7 at 12:00 LT, although its standard deviation is smaller than that of the CATS throughout the whole day. The ISCCP, which is the closest dataset to the regional mean total cloud cover of the CATS in Fig. 2, has a standard deviation of spatial series that is similar to that of the CATS and a correlation coefficient larger than half of the datasets most of the time. It should be noted that the correlation coefficient between the ISCCP and CATS at 09:00 LT and 18:00 LT is only approximately 0.2. Fig. 1 shows that the regional distribution of large values between these two satellites is obviously distinct. The standard deviation in the Himawari-8 is the largest from 06:00 LT to 12:00 LT, which indicates that the Himawari-8 overestimates the spatial difference when the mean total cloud cover is relatively low. The MAE is also larger during this time (Fig. S1). However, in general, the spatial distribution of total cloud cover detected by the CATS and the Himawari-8 is consistent, with a correlation coefficient of approximately 0.5. Despite the different amplitudes of diurnal variation in total cloud cover between the CATS and the reanalysis dataset, their spatial distribution shows high consistency, with a correlation coefficient of up to 0.8 for the MERRA-2 at 06:00 LT. The standard deviation of the ERA5 and MERRA-2 is less than that of the CATS during the whole day except at 03:00 LT. From 18:00 LT to 03:00 LT, the MAE between the ERA5 and the CATS is the smallest (Fig. S1).

3.2 Diurnal cycle of cloud vertical distribution

The vertical structure of clouds is closely related to precipitation and cloud radiative effects, which has attracted widespread attention (Yan et al., 2016; Wang et al., 2000; Li et al., 2018). Moreover, the cloud vertical structure is an



290 important factor in studying how climate change influences cloud feedback (Wang et al., 2000; Bodas-Salcedo, 2018). Until recently, information about cloud vertical structure was usually extracted from surface observations, such as radiosonde data, which can provide four of five decades of records for climate research (Wang and Rossow, 1995). Since the launch of CALIPSO and CloudSat, active satellite data have been widely used in the study of global cloud vertical structures (Oreopoulos et al., 2017). However, the limited observation times each day from the CALIPSO/CloudSat result in an unclear

295 diurnal cycle of cloud vertical distribution over the TP. In a recent study, Noel et al. (2018) first used the CATS to analyse the diurnal cycle of cloud profiles over land and oceans between 51°S and 51°N and found similar vertical distributions of cloud cover between CATS and CALIPSO at a near-global scale. In this section, we compare the cloud vertical distribution of different subregions using the CATS, ERA5 and MERRA-2. As a reference, the spatio-temporal matched cloud vertical profiles from CALIPSO alone and the combined product from CALIPSO and CloudSat (that is, 2B-GEOPROF-lidar, marked as CALIPSO & CloudSat in Fig. 4) are also used. Fig. 4 provides the cloud vertical profiles at 13:30 LT, and the results during different seasons at this time are given in Fig. S2. From the averaged cloud vertical distribution over the whole TP region (Fig. 4a), CATS, CALIPSO, ERA5 and CloudSat & CALIPSO exhibit consistent peak heights (approximately 8 km) of cloud cover, whereas MERRA-2 overestimates the peak height of cloud cover (approximately 11 km). Similarly to Noel et al. (2018), we also find that the cloud vertical profiles from CALIPSO agree well with those from CATS, especially

300 over the northwestern and southeastern parts of the TP (Fig. 4b and Fig. 4e). The small difference between CATS and CALIPSO possibly comes from the spatio-temporal matching process, mostly. Such agreement between CATS and CALIPSO is understandable because CATS employs an atmospheric layer detection algorithm similar to that of CALIOP (Yorks et al., 2016). This means that they also have similar detection limitations; for example, they cannot penetrate optically thick clouds to detect the underlying clouds and thus underestimate cloud cover at low atmosphere levels. The 2B-GEOPROF-lidar combines the advantages of CALIPSO and CloudSat in detecting both optically thin and thick cloud systems and thus can provide a relatively accurate cloud vertical distribution compared to other datasets. Indeed, compared with 2B-GEOPROF-lidar, the CATS and CALIPSO datasets obviously underestimate the cloud cover at middle and low atmosphere levels, and the bias of cloud cover even reaches 0.3 and 0.2 at 8 km and 4 km over the southeastern TP (Fig. 4e), respectively. In particular, the bias between CATS (or CALIPSO) and the 2B-GEOPROF-lidar product is more obvious

305 during the spring and summer seasons (Fig. S2). At the middle level of the atmosphere, cloud cover differences between CATS (or CALIPSO) and 2B-GEOPROF-lidar may result from altocumulus, altostratus or deep convective clouds. However, at the low level of the atmosphere, their cloud cover difference mainly comes from the undetected cumulus or status clouds in the CATS due to lidar signal attenuation, especially over the southeastern part of the TP (Fig. 4e), where surface wind convergence and upwards motion forced by topography tend to promote cumulus clouds (Li and Zhang, 2016).

315

320 The peak cloud covers from the reanalysis datasets are obviously lower than those detected by active satellites. Moreover, the peak heights are also different between the reanalysis datasets. The ERA5 has a peak cloud cover (approximately 0.2) at 8 km over the western TP, whereas the peak height exceeds 9 km over the northeastern TP. Fig. 4a clearly shows that an important peak cloud cover exists at low atmosphere levels (<4 km) in the ERA5 over the whole TP.



This peak is particularly obvious over the southern part of the TP (Fig. 4d and 4e). Over the southwestern TP (Fig. 4d), the
325 ERA5 obviously overestimates the cloud cover compared with the 2B-GEOPROF-lidar below 4 km, but the other datasets
maintain a consistently low cloud cover, especially during the summer and autumn seasons (Fig. S2c and S2d). One possible
cause might be that the very large terrain causes a very large model bias in the vertical cloud distribution of the ERA5 model,
which is also found in the ERA-interim (Yin et al., 2015). Over the southeastern TP (Fig. 4e), although ERA5 and 2B-
GEOPROF-lidar both exhibit a second peak cloud cover below 4 km, the height of the peak value is significantly
330 underestimated by the ERA5. In contrast to the cloud cover retrieval by satellites, the ERA5 prognosticates a grid box
fractional cloud cover by parameterizing cloud formation and evolution processes that consider cumulus updrafts, vertical
motions, diabatic cooling, etc. (ECMWF, 2016). By comparing the vertical cloud structure of warm conveyor belts in the
ERA5 and CloudSat/CALIPSO datasets, Binder et al. (2020) found that the ERA5 represents the frozen hydrometeor
distribution well but underestimates the high ice and snow values in the mixed-phase clouds near the melting layer. In
335 addition, they point out that many small and mesoscale structures observed by remote sensing instruments are not captured
by the ERA5. Similar to total cloud cover, the vertical profile of cloud cover in the MERRA-2 is also obviously
underestimated, but the height of the peak value is consistently overestimated for all subregions. This phenomenon is also
found in the tropics, where the MERRA-2 succeeds in representing high-level clouds but dramatically underestimates low-
and mid-level clouds (Miao et al., 2019). The critical relative humidity, which is the humidity threshold for cloud formation
340 in the estimation of cloud cover in MERRA-2, is possibly responsible for the bias (Yeo et al., 2022; Molod, 2012). Finally,
these biases will exacerbate the uncertainties in the heating rate profiles of MERRA-2 and ERA5.

After realizing the intrinsic uncertainties of different datasets in characterizing the cloud vertical distribution, the
diurnal cycles of cloud vertical distribution over different subregions from CATS, ERA5 and MERRA-2 are further
compared in Fig. 5. Fig. 4 shows a significant underestimation of cloud cover in the ERA5 and MERRA-2 datasets
345 compared with CATS at a given time. In fact, the underestimation is persistent throughout the day (see Fig. 5). Over the
northern part of the TP, clouds are distributed in a relatively narrower height range (e.g., from 4 km to 14 km) than those
over the southern part of the TP (e.g., from 4 km to 18 km), which may be linked to the deep convective clouds or cirrus
clouds over the northern part. Over the northwestern TP, the cloud cover at approximately 8 km reaches its maximum value
(approximately 0.3) of the day, which is sustained from 12:00 LT to 06:00 LT for CATS. In the ERA5, the maximum cloud
350 cover at approximately 8 km is approximately 0.25, and this value is sustained only from 15:00 LT to 00:00 LT.
Considerable differences in the cloud cover between the CATS and ERA5 mainly occur during nighttime. Two points need
to be emphasized. First, the ERA5 captures clouds above 12 km from 18:00 LT to 03:00, which is consistent with the CATS.
Second, the ERA5 also exhibits more low-level clouds below 4 km during the night. This phenomenon is particularly
obvious over the southern part of the TP. For example, low-level clouds have a maximum of 0.2 over the southeastern TP
355 and persist from 18:00 LT to 09:00 LT. Recent ground-based cloud vertical structure observations indicate that the cloud
base height has an obvious peak at 1.5 km-3.5 km for the whole day, and the frequency is greater at night in the dry seasons
over the southeastern TP (Zhou et al., 2021). The formation of low clouds over the TP is thought to be favoured by low air



density and strong turbulence (Xu, 2012) and associated with large-scale convergence and planetary boundary layer processes (Li and Zhang, 2016). By using CloudSat–CALIPSO datasets, Kukulies et al. (2019) also point out that the stratocumulus and cumulus clouds dominate low-level clouds over the TP, and there are more stratocumulus clouds during the monsoon season (May to September) and more cumulus clouds during the westerly season (October to April). This observation verifies the inability of the CATS to detect the vertical structure of low clouds or optically thick clouds, but the persistent low clouds over the southwestern TP in the ERA5 may also be problematic (also see Fig. 4d). In addition to low-level clouds, a large difference in the diurnal cycle of cloud cover is obvious at approximately 8 km over the southern TP. The ERA5 and MERRA-2 models cannot reproduce the distribution nor the magnitude of the diurnal cycle of cloud cover over the southwestern TP. For example, the CATS observes a high cloud cover at 14 km at approximately 18:00 LT, but the ERA5 misses it and cannot capture the cloud vertical distribution after 21:00 LT. Compared with the ERA5, the MERRA-2 model has a poorer performance in reproducing the diurnal cycle of cloud cover, with larger biases in both the maximum cloud cover and its height. Here, it is worth noting that although the CATS also obviously underestimates the cloud cover at almost every height compared with the 2B-GEOPROF-lidar (see Fig. 4), it can still capture the pattern of the cloud vertical distribution and the corresponding height of the peak cloud cover except at a low atmosphere level (see Fig. 4). This means that a qualitative assessment of cloud cover at middle- and high atmosphere levels (e.g., peak cloud cover at 8 km) from reanalysis products with CATS observations is still feasible. In addition, the red lines at the top of Fig. 5 represent the diurnal variation in tropopause height. It is clear that some clouds can penetrate the tropopause over the TP, which is a large terrain with a high altitude. The diurnal variation in the clouds overshooting the tropopause will be explored in Fig. 7 in the next section.

3.3 Diurnal variations of cirrus and overshooting clouds

Due to the high sensitivity of lidar signals to cirrus clouds, space-based lidar is considered an irreplaceable tool in detecting cirrus clouds and their vertical distribution at a global scale, especially in the upper troposphere and lower stratosphere (Fu et al., 2007; Virts et al., 2010). As an important cloud type, cirrus clouds play an important role in influencing the Earth’s radiation budget and accurately calculating the heating rate (Liou, 1986; Hartmann et al., 2001). A recent study suggests that changing the physical properties of cirrus clouds may even counteract global warming. By seeding cirrus clouds with efficient ice nucleating particles, which may shorten their lifetime and make them more transparent, the increase in global mean surface temperature projected with $1.5\times\text{CO}_2$ concentrations is counteracted by 70% in the CESM–CAM5 model (Gasparini et al., 2020). In addition, cirrus clouds can affect ozone concentrations in the upper troposphere and lower stratosphere (UT/LS) by acting as a potential surface for heterogeneous reactions (Borrmann et al., 1996). Similar to the cirrus classification method of Sassen et al. (2009), this study defines cirrus clouds as clouds whose cloud top temperature is less than $-40\text{ }^\circ\text{C}$. Based on their optical thickness (TAU), cirrus clouds may be further divided into three types: subvisible cirrus ($\text{TAU}<0.03$), thin cirrus ($0.03<\text{TAU}<0.3$) and opaque cirrus ($0.3<\text{TAU}<3$) clouds (Sassen and Cho, 1992). Previous studies have investigated the radiative effect of these different cirrus cloud types. For example, Fusina et al. (2007)



found that the differences in heating rates between thin cirrus clouds and ice supersaturated regions can reach up to 15 K d^{-1} at the meteorological observatory in Lindenberg, Germany. By matching the observations of CERES, MODIS and CALIPSO satellites, Sun et al. (2011a) point out that cirrus clouds whose optical depth is less than 0.3 have a significant cooling effect on shortwave radiation by increasing the diurnal mean reflected shortwave flux by approximately 2.5 W m^{-2} , and clouds with an optical depth of 0.1 can have a warming effect of approximately 15 W m^{-2} . In addition, the subvisible cirrus clouds with significant positive radiative forcing have recently received much attention after the establishment of many effective detection methods (Sun et al., 2015; Sun et al., 2014).

Until now, however, few studies have focused on the diurnal cycle of cirrus clouds, especially over the TP region. In the simulation of the life cycle of anvil cirrus clouds, Gasparini et al. (2019) found that adding the diurnal variations of solar radiation would affect the evolution and radiative effects of cirrus. In this section, we further use the observational advantage of the CATS to discuss the diurnal cycle of cloud cover of cirrus clouds with different optical depths over the TP region (Fig. S3). In addition, the seasonal variation and diurnal cycle of regional averaged cloud cover for different cirrus types are provided in Fig. 6. Opaque cirrus clouds (Fig. 6d) are found to be the main components of total cirrus clouds (Fig. 6a), and their diurnal cycles are similar. The peak cloud cover of opaque cirrus clouds occurs at 15:00 LT over the northeastern TP, where its value may reach 0.24 (see Fig. S3d). Over the southwestern TP, opaque cirrus occur less frequently than over the central and northeastern parts. After 15:00 LT, opaque cirrus clouds gradually decrease and have a minimum value of 0.09 at 09:00 LT (see Fig. 6d). Opaque cirrus clouds usually occur more frequently during the spring season and less frequently during autumn. In addition, they are more likely to occur at 15:00-18:00 LT, and their daily range even exceeds 0.2 during spring (Fig. 6d). Compared with other cirrus cloud types, the cloud cover of subvisible cirrus clouds is smallest, and its peak time is obvious later than that of opaque cirrus clouds (Fig. 6b). On average, subvisible cirrus clouds have a maximum regional averaged cloud cover (approximately 0.08) at 03:00 LT and a minimum value of 0.03 at 09:00 LT. In contrast to opaque cirrus clouds, subvisible cirrus clouds tend to occur at 18:00-24:00 LT in the summer season and at 03:00 LT in the spring season (see Fig. 6b). These statistical results above show that subvisible and opaque cirrus clouds over the TP are more frequent during nighttime and daytime, respectively. Based on the limited observations from two overpass times of the CALIPSO and CloudSat satellites, Sassen et al. (2009) also indicate that opaque cirrus clouds are generally found during the daytime, whereas subvisible cirrus clouds are mainly found at night. For thin cirrus clouds, although their diurnal cycle is not as significant as that of the other two kinds of cirrus clouds (Fig. 6c and Fig. S3c), the maximum cloud cover at 03:00 LT and minimum cloud cover at 09:00 LT are still obvious. Generally, there are more cirrus clouds in spring, and the cloud cover of total cirrus clouds is the smallest in autumn. Moreover, the diurnal cycles of different cirrus cloud types cancel each other and decrease the amplitude of the diurnal cycle of cirrus clouds, especially at 15:00-03:00 LT (Fig. 6a). On average, the cirrus cloud cover over the TP is mainly comprised of opaque cirrus clouds, followed by thin cirrus clouds, and subvisible cirrus clouds are the least common. This result is different from those of other regions (e.g., northern South America, equatorial Africa, and the western Pacific) according to Sassen et al. (2009), who found that the thin cirrus category comprises the majority of global cirrus clouds, followed by subvisible cirrus clouds, and opaque cirrus clouds are



425 the least common. These results also reflect the regional difference in different cirrus types, which is possibly linked to several potential cirrus cloud formation mechanisms (e.g., radiative cooling in moist upper-tropospheric layers, convective blow-off, and temperature perturbation caused by convective activities such as gravity waves) (Zhang et al., 2020a; Heymsfield et al., 2017; Ramaswamy and Detwiler, 1986).

Previous studies indicate that some clouds can penetrate the tropopause into the stratosphere, especially over the TP, where tropopause folding events can reach 80% during certain winters (Chen et al., 2011), and these events are always accompanied by overshooting convective systems (Tian et al., 2020). Overshooting clouds driven by convection activities can affect the material exchange between tropospheric and stratospheric signals (Tian et al., 2011) and can exacerbate the greenhouse effect and increase polar ozone consumption (Kirk-Davidoff et al., 1999; Forster and Shine, 2002; Luo et al., 2011). In particular, the impact of overshooting convection on stratospheric water vapour depends on the hour timescale (Dauhut et al., 2020). Here, we also preliminarily analyse the diurnal cycle of cloud cover above the tropopause in different subregions of the TP across different seasons (see Fig. 7). Similarly to the methods of Dauhut et al. (2020), we consider only clouds with a base in the tropopause and a top in the stratosphere as overshooting clouds.

The results indicate that the cloud cover above the tropopause is higher at night and concentrated over the southwestern TP (Fig. 7a). The average cloud cover of overshooting clouds over the southwestern TP is 4.76×10^{-3} , accounting for approximately half of the total. In addition to the peaks in overshooting cloud cover at approximately 22:00 LT and approximately 03:00 LT, there is a secondary peak in the afternoon at approximately 14:00 LT (over the southeast). Among the different seasons, the average cloud cover above the tropopause in summer is the largest, with an average of 2.75×10^{-3} , approximately three times that in winter, although the daily peaks in cloud cover vary slightly throughout the year. The nighttime peak of the overshooting cloud cover occurs earliest in summer (19:00 LT) and latest in spring (02:00 LT). Additionally, based on CATS data, Dauhut et al. (2020) explored the diurnal cycle of tropical overshooting clouds and found that cloud cover has a first peak at 19:00 or 20:00 LT and a second peak at 00:00 or 01:00 LT. There is no afternoon peak in cloud cover, indicating that the lower tropopause of the TP can promote cloud formation by the afternoon thermal convection penetrating the tropopause, but this is not evident in the tropical region.

3.4 Meteorological factors associated with total cloud cover and cirrus clouds

450 The diurnal variation in cloud cover is closely related to the diurnal variations of meteorological fields, which promote or inhibit cloud formation (Lei et al., 2020; Feofilov and Stubenrauch, 2019). In this section, we further analyse the correlation of the standardized diurnal cycle between the total cloud cover (and cirrus cover) in the CATS dataset and related meteorological factors in the ERA5 dataset (e.g., 2-m temperature, 10-m wind speed, and vertically integrated divergence of moisture flux) over different regions of the TP (see Fig. 8). The statistical results suggest that the total cloud cover is strongly correlated with the 2-m temperature, 10-m wind speed, and vertically integrated divergence of moisture flux, regardless of region. The total cloud cover, 2-m temperature and 10-m wind speed almost always peak in the afternoon



(approximately 15:00 LT), although their peaks do not coincide perfectly. Conversely, the vertically integrated divergence of moisture flux reaches its daily lowest value in the afternoon (approximately 15:00 LT). Among all factors and regions, the correlation between the total cloud cover and the 2-m air temperature is the strongest over the northeastern TP (Fig. 8b), with a correlation coefficient of 0.83. The absolute values of the correlation coefficients between the meteorological factors and the total cloud cover all exceed 0.4, and all of them pass the 90% significance test. In fact, the relationship between the diurnal variations of cloud cover and meteorological factors can be explained mainly by the dynamic and thermal processes of cloud formation and involves processes at different levels of the atmosphere (Kuang and Bretherton, 2006). For example, previous studies have indicated that strong wind near the surface facilitates the transport of moist air at low levels, whether it comes from the Indian Ocean in winter or from the surrounding convergence in summer (Yan et al., 2016). Abundant water vapour is beneficial to cloud formation, which also explains the influence of the vertically integrated divergence of moisture flux on cloud cover. In addition, solar warming of the surface powers the lifting of air masses, which can produce a buoyantly unstable layer near the surface and promote cloud formation, especially of convective boundary layer clouds (Angevine et al., 2001). However, we know that these dynamic and thermal processes between clouds and meteorological factors are coupled, which means that meteorological factors are both linked to the formation of clouds and affected by the clouds (Betts et al., 2014). Thus, the correlation analyses above provide only limited insights into the effects of different meteorological parameters on the total cloud cover diurnal cycle, but they cannot be used to prove a robust causal relationship between them.

The diurnal variations of cloud cover and meteorological factors vary at the lower and upper tropopause and are driven by different mechanisms (Chepfer et al., 2019). Using ground-based remote sensing data, Mace et al. (2006) found that cirrus clouds are more likely to form in the ascending region of the upper troposphere during the cold season, and in summer, the formation of cirrus clouds is also always linked to detrainment from deep convection with both vertical motion and humidity anomalies. The detrainment from deep convection accompanied by small-scale condensate mass updrafts can form cirrus clouds (Mace et al., 2006). In addition, mid-latitude weather disturbances with gentle ascending motion are associated with the formation of cirrus clouds (Heymsfield, 1977), and the generation of local convective instabilities also promotes cirrus formation (Sassen et al., 1989). Thus, cirrus formation mechanisms include the supersaturating of water vapour caused by the lifting of the air parcel (e.g., large-scale front, small-scale vertical circulations, convective clouds, and gravity waves) or by radiational cooling (Heymsfield et al., 2017). The above formation mechanisms of cirrus clouds are partly linked to related meteorological variables (e.g., 250 hPa relative humidity, 2-m temperature, and 250 hPa vertical velocity). Thus, the relationship between the diurnal variations of regional averaged cirrus clouds and these parameters is explored in Fig. 9. Only the meteorological factor curves for which the correlation with cirrus clouds pass the significance test by 90% are shown. The results show that the peak time of the cloud cover of different cirrus types are different to some extent, as subvisible cirrus clouds (Fig. 9b) peak at midnight (03:00 LT), but the cloud cover of opaque cirrus clouds (Fig. 9d) is greater in the afternoon (15:00 LT). Therefore, different cirrus cloud types have different correlations with different meteorological factors. The correlation coefficient between the diurnal variations of subvisible cirrus clouds and 250 hPa



relative humidity reaches 0.86 (Fig. 9b), indicating that the formation of subvisible cirrus clouds possibly depends on abundant water vapour. As shown from the spatial distribution of the correlation coefficient (Fig. S4b), in most areas of the TP, subvisible cirrus clouds have a positive correlation with water vapour, with a correlation coefficient greater than 0.3, whereas the correlation with the other two factors (2-m temperature and 250 hPa vertical velocity, shown in Figs. S4f and 495 S4j, respectively) is significant only in a small part of the region, and the correlation is weak. There are clear peaks in the cloud cover of thin cirrus clouds both in the afternoon and at midnight (Fig. 9c), and thin cirrus clouds have a weak positive correlation with relative humidity (correlation coefficient of 0.42) and vertical velocity (correlation coefficient of 0.34). From the small-scale results of each 2° grid, thin cirrus clouds have a significant positive correlation with relative humidity only in the northern TP (Fig. S4c) and a positive correlation (correlation coefficient of approximately 0.4) with vertical 500 velocity in the northwestern TP (Fig. S4k). Feofilov and Stubenrauch (2019) found that the formation of cirrus clouds with a cloud emissivity between 0.1 and 0.5 may be partly due to the water vapour released by the dispersal of deep convection anvil clouds. Chepfer et al. (2019) also found a consistency between the diurnal cycle of relative humidity and cirrus clouds (with optical depths below 3 to 5) in the free troposphere, but their joint evolution is likely driven by the diurnal variations of surface temperature rather than the change in the amount of water vapour in the atmosphere. However, the 2-m temperature 505 do not exhibit a significant correlation with subvisible and thin cirrus clouds in our study. Conversely, the diurnal variations of opaque cirrus clouds are positively correlated only with the 2-m temperature and 250 hPa vertical velocity (correlation coefficients of 0.77 and 0.53, respectively), whereas they have no significant correlation with relative humidity change (Fig. 9d). This phenomenon can be explained by the more frequent deep convective activities promoted by higher surface temperatures (Igel et al., 2014). In addition, cirrus cloud formation is closely associated with deep convective activities 510 (Sassen et al., 2009). The statistical results of the small-scale region also show a strong positive correlation between opaque cirrus clouds and the 2-m temperature in the whole TP (Fig. S4h). However, there is an inconsistent correlation between these clouds and vertical velocity in different areas (Fig. S4l), perhaps because of the great difference in the spatial distribution of diurnal variations of vertical velocity over the TP. The above result suggests that the formation of relatively thick cirrus clouds is more sensitive to air mass uplift, which is linked to convective instabilities driven by thermal 515 conditions of the surface and intense vertical motion. In summary, after averaging the cloud cover of all cirrus cloud types, the total cirrus cloud cover is positively correlated with all these meteorological factors at a 90% confidence level. Among these factors, total cirrus cloud cover has the strongest correlation with the 250 hPa relative humidity, with a correlation coefficient of 0.61. Moreover, as shown in the spatial distribution of the correlation coefficients between meteorological factors and total cirrus clouds in Fig. S4 (a, e, i), only the 250 hPa relative humidity shows a positive correlation with the 520 diurnal variations of total cirrus cloud cover over most of the TP.



4 Conclusions and discussion

The TP, also known as the “Asian water tower”, has experienced significant climate changes that are closely linked to clouds. Much of the existing research has focused on long-term changes in cloud properties. However, the diurnal variation in clouds, which plays an important role in the energy budget of the Earth-atmospheric system and climate change, has still received insufficient attention due to observation limitations. As a result, this study explores the diurnal cycle of clouds over the TP based on CATS, ISCCP, Himawari-8, ERA5, MERRA-2, and CMIP6 outputs. The main results are as follows:

1. The total cloud cover over the TP peaks at 12:00-15:00 LT, and clouds are concentrated over the eastern TP. The CATS satellite can capture more clouds at night, as lidar can recognize more of the optical thin cirrus clouds that occur frequently at night than can passive detectors. The largest amplitude of diurnal variations is detected by the Himawari-8, but the diurnal cycle of cloud cover from reanalysis and CMIP6 models does not show changes as dramatic as those from satellite observations.
2. Compared with the cloud vertical distribution detected by the CATS, the results from ERA5 and MERRA-2 show significant underestimation of cloud cover at middle- and high- atmosphere levels. At night, there are more clouds concentrated near the surface over the southern TP according to the reanalysis results, but the CATS lidar has difficulty identifying low clouds under thick clouds. Therefore, the CATS cannot obtain complete information on the diurnal variations of cloud vertical distribution over the southeastern TP, where low-level clouds are concentrated. However, the CATS can still capture the pattern in cloud vertical distribution and the corresponding height of peak cloud cover at middle- and high- atmosphere levels.
3. The cloud cover of opaque cirrus clouds ($0.3 < \text{optical thickness} < 3$) dominates other cirrus cloud types over the TP and peak at 15:00 LT over the northeastern TP. These cirrus clouds show different characteristics from cirrus clouds in the tropics, where thin cirrus clouds dominate (Sassen et al., 2009). More thin cirrus clouds occur at night, especially in the spring. The seasonal average cloud cover of subvisible cirrus clouds (optical thickness < 0.03) peaks at 03:00 LT. Over 7% of the subvisible cirrus clouds exist at night (21:00-03:00 LT), which is difficult to detect using passive methods. Over the southwestern TP, over 2% of clouds can penetrate the tropopause at 22:00 LT and 02:00 LT, affecting the material exchange between the tropospheric and stratospheric regions.
4. The diurnal variations of the vertically integrated divergence of moisture flux, 2-m temperature and 10-m wind speed show strong correlations with diurnal variations of total cloud cover over the TP. The diurnal cycle of subvisible cirrus clouds has a strong correlation with the 250 hPa relative humidity over the whole TP, which indicates that the diurnal variations of cirrus clouds are more dependent on the variations in water vapour than the variations in other factors. However, the diurnal variations of opaque cirrus clouds are obviously affected by the 2-m temperature and 250 hPa vertical velocity, which shows a connection between the formation of relatively thick cirrus clouds and air mass uplift. The diurnal cycle of thin cirrus clouds shows a relatively weak correlation with the diurnal cycle of relative humidity and vertical velocity.



555 The comparison of the diurnal cloud cycle between different datasets in this study suggests that large differences exist
in these datasets over the TP. Indeed, compared with those of satellites, the amplitudes of cloud diurnal variations obtained
by reanalysis and CMIP6 models are too small to affect the simulation of radiation. The large differences and uncertainties in
the diurnal cloud cycle between these datasets will undoubtedly affect the prediction and attribution of future climate change.
The following problems contribute to the inconsistency of total cloud cover: (1) Detection sensitivity: modern passive
satellites still have difficulty identifying high-level thin clouds and usually misclassify these clouds as clear sky. (2) Cloud
560 parameterization: some cloud parameterization schemes in climate models and reanalysis data are unreasonable and need to
be further improved. (3) Discrepancies in the definitions of cloud cover between observations and models. In addition, the
different temporal scales of sampling and the different quantification algorithms of cloud cover may lead to differences
between satellite retrievals and model simulations (Engström et al., 2015). In recent years, many studies have contributed to
reducing the uncertainty of observed and simulated cloud cover. For example, Sun et al. (2014 and 2015) found that using
565 the polarization angle feature of backscattered solar radiation, super thin cirrus clouds with an optical thickness of ~ 0.06 can
be effectively detected. This offers a new approach for detecting subvisible clouds based on low-cost passive instruments.
For the uncertainties in the reanalysis datasets and the other models, the accuracy of model simulations can be improved by
optimizing the physical process descriptions in parameterized schemes. The total cloud cover simulated by the new explicit
prognostic cloud cover scheme (PROGCS) in GRAPES_GFS is more realistic and directly links cloud cover to the physical
570 processes of cloud formation (e.g., cumulus convection) instead of achieving cloud cover as a function of relative humidity
and the condensate mixing ratio (Ma et al., 2018). In addition, the improvement in cloud overlap parameterization might help
to optimize the simulation of cloud cover in multilayer cloud scenarios (Li et al., 2019; Li et al., 2018). Meantime, the
ground observations in regional large-scale comprehensive observation experiments greatly help to explore the mechanisms
of cloud diurnal variations and to improve the model simulations (Ge et al., 2019; Yang et al., 2021).

575 In this study, the diurnal cycles of cirrus clouds with different optical depths are explored. Some recent studies have
also further discussed the regulatory and formation mechanisms of the diurnal cycle of cirrus clouds. For example, Gasparini
et al. (2019) indicate that the diurnal variations of insolation can regulate anvil cirrus evolution and radiative effects. For
stratospheric cirrus over the Great Plains and surrounding areas, Zou et al. (2021) found that they are mainly developed by
deep convection and gravity wave events. By using the CALIPSO observation and reanalysis dataset, Zhang et al. (2021)
580 point out that large-scale topographic uplift, ice particle production due to temperature fluctuations, and residuals from deep
convective anvils contribute to summer cirrus cloud formation over the TP at locations under 9 km, 9-12 km, and above 12
km, respectively. However, these dynamic mechanisms of cirrus formation are complex and cannot be completely described
in the diurnal cycle. Thus, although the amount of cirrus cloud cover over the TP is related to meteorological factors from
the perspective of microphysics, the present analysis still cannot provide a clear interpretation of which mechanisms drive
585 the diurnal cycles of cirrus clouds of different optical depths. Further comprehensive investigations are still needed. In
addition, this study considers only a few typical meteorological factors. There are other factors (e.g., aerosol loading) that



impact the diurnal variations of the cloud amount that should also be considered in future studies (Ntwali and Chen, 2018; Matsui et al., 2006).

Data availability

590 The CATS datasets are downloaded from the NASA Langley Research Center Atmospheric Science Data Center (ASDC) website: <https://eosweb.larc.nasa.gov/project/CATS-ISS?level=2>. The ISCCP data is available from website: <https://www.ncei.noaa.gov/products/international-satellite-cloud-climatology>. The Himawari-8 data is available from the Japan Aerospace Exploration Agency, Earth Observation Research Center (JAXA/EORC) website: <https://www.eorc.jaxa.jp/tree/>. The ERA5 datasets is available from Climate Data Store (CDS) website: <https://cds.climate.copernicus.eu/cdsapp#!/home>. The MERRA-2 datasets is available from the Global Modeling and Assimilation Office (GMAO) website: <https://gmao.gsfc.nasa.gov/reanalysis/MERRA-2/>. The CMIP6 outputs is downloaded from the Earth System Grid Federation (ESGF) website: <https://esgf-node.llnl.gov/search/cmip6/>.

Competing interests

600 Some authors are members of the editorial board of journal Atmospheric Chemistry and Physics. The peer-review process was guided by an independent editor, and the authors have also no other competing interests to declare.

Author contribution

YZ and JL organized the paper and carried them out. YZ prepared the manuscript with contributions from all co-authors. JL conceptualized the paper and revised the whole manuscript. LZ, CD and YL downloaded the data and maintain research data. YH, BJ and JH provided suggestions for this study. All authors contributed to the discussion of the results and reviewed the manuscript.

Acknowledgements

This research was jointly supported by the Strategic Priority Research Program of the Chinese Academy of Sciences (XDA2006010301) and the National Science Fund for Excellent Young Scholars (42022037). We would like to thank the CATS, ISCCP, Himawari-8, ERA5, MERRA-2 and CMIP6 science teams for providing excellent and accessible data products that made this study possible.



References

- Angevine, W. M., Baltink, H. K., and Bosveld, F. C.: Observations Of The Morning Transition Of The Convective Boundary Layer, *Bound.-Layer Meteor.*, 101, 209-227, <https://doi.org/10.1023/A:1019264716195>, 2001.
- 615 Betts, A. K., Desjardins, R., Worth, D., and Beckage, B.: Climate coupling between temperature, humidity, precipitation, and cloud cover over the Canadian Prairies, *J. Geophys. Res.-Atmos.*, 119, 13,305-313,326, <https://doi.org/10.1002/2014JD022511>, 2014.
- Binder, H., Boettcher, M., Joos, H., Sprenger, M., and Wernli, H.: Vertical cloud structure of warm conveyor belts – a comparison and evaluation of ERA5 reanalysis, CloudSat and CALIPSO data, *Weather Clim. Dynam.*, 1, 577-595, <https://doi.org/10.5194/wcd-1-577-2020>, 2020.
- 620 Bodas-Salcedo, A.: Cloud Condensate and Radiative Feedbacks at Midlatitudes in an Aquaplanet, *Geophys. Res. Lett.*, 45, 3635-3643, <https://doi.org/10.1002/2018GL077217>, 2018.
- Borrmann, S., Solomon, S., Dye, J. E., and Luo, B.: The potential of cirrus clouds for heterogeneous chlorine activation, *Geophys. Res. Lett.*, 23, 2133-2136, <https://doi.org/10.1029/96GL01957>, 1996.
- Chen, X. L., Ma, Y. M., Kelder, H., Su, Z., and Yang, K.: On the behaviour of the tropopause folding events over the Tibetan Plateau, *Atmos. Chem. Phys.*, 11, 5113-5122, <https://doi.org/10.5194/acp-11-5113-2011>, 2011.
- 625 Cheng, G. and Wu, T.: Responses of permafrost to climate change and their environmental significance, Qinghai-Tibet Plateau, *J. Geophys. Res.*, 112, <https://doi.org/10.1029/2006JF000631>, 2007.
- Chepfer, H., Brogniez, H., and Noel, V.: Diurnal variations of cloud and relative humidity profiles across the tropics, *Sci. Rep.*, 9, 16045, <https://doi.org/10.1038/s41598-019-52437-6>, 2019.
- 630 Cherian, R. and Quaas, J.: Trends in AOD, Clouds, and Cloud Radiative Effects in Satellite Data and CMIP5 and CMIP6 Model Simulations Over Aerosol Source Regions, *Geophys. Res. Lett.*, 47, e2020GL087132, <https://doi.org/10.1029/2020GL087132>, 2020.
- Dai, A. and Trenberth, K. E.: The Diurnal Cycle and Its Depiction in the Community Climate System Model, *J. Clim.*, 17, 930-951, [https://doi.org/10.1175/1520-0442\(2004\)017<0930:Tdcaid>2.0.Co;2](https://doi.org/10.1175/1520-0442(2004)017<0930:Tdcaid>2.0.Co;2), 2004.
- 635 Dauhut, T., Noel, V., and Dion, I. A.: The diurnal cycle of the clouds extending above the tropical tropopause observed by spaceborne lidar, *Atmos. Chem. Phys.*, 20, 3921-3929, <https://doi.org/10.5194/acp-20-3921-2020>, 2020.
- Duan, A. and Wu, G.: Change of cloud amount and the climate warming on the Tibetan Plateau, *Geophys. Res. Lett.*, 33, <https://doi.org/10.1029/2006GL027946>, 2006.
- ECMWF: IFS Documentation CY41R2 - Part IV: Physical Processes, in: IFS Documentation CY41R2, IFS Documentation, 4, ECMWF, 2016.
- 640 Engström, A., Bender, F. A.-M., Charlson, R. J., and Wood, R.: The nonlinear relationship between albedo and cloud fraction on near-global, monthly mean scale in observations and in the CMIP5 model ensemble, *Geophys. Res. Lett.*, 42, 9571-9578, <https://doi.org/10.1002/2015GL066275>, 2015.



- Eyring, V., Bony, S., Meehl, G. A., Senior, C. A., Stevens, B., Stouffer, R. J., and Taylor, K. E.: Overview of the Coupled
645 Model Intercomparison Project Phase 6 (CMIP6) experimental design and organization, *Geosci. Model Dev.*, 9, 1937-1958, <https://doi.org/10.5194/gmd-9-1937-2016>, 2016.
- Feofilov, A. G. and Stubenrauch, C. J.: Diurnal variation of high-level clouds from the synergy of AIRS and IASI spaceborne infrared sounders, *Atmos. Chem. Phys.*, 19, 13957-13972, <https://doi.org/10.5194/acp-19-13957-2019>, 2019.
- Forster, P. M. d. F. and Shine, K. P.: Assessing the climate impact of trends in stratospheric water vapor, *Geophys. Res. Lett.*,
650 29, <https://doi.org/10.1029/2001GL013909>, 2002.
- Fu, Q., Hu, Y., and Yang, Q.: Identifying the top of the tropical tropopause layer from vertical mass flux analysis and CALIPSO lidar cloud observations, *Geophys. Res. Lett.*, 34, <https://doi.org/10.1029/2007GL030099>, 2007.
- Fusina, F., Spichtinger, P., and Lohmann, U.: Impact of ice supersaturated regions and thin cirrus on radiation in the midlatitudes, *J. Geophys. Res.-Atmos.*, 112, <https://doi.org/10.1029/2007JD008449>, 2007.
- 655 Gasparini, B., McGraw, Z., Storelmo, T., and Lohmann, U.: To what extent can cirrus cloud seeding counteract global warming, *Environ. Res. Lett.*, 15, <https://doi.org/10.1088/1748-9326/AB71A3>, 2020.
- Gasparini, B., Blossey, P. N., Hartmann, D. L., Lin, G., and Fan, J.: What Drives the Life Cycle of Tropical Anvil Clouds?, *J. Adv. Model. Earth Syst.*, 11, 2586-2605, <https://doi.org/10.1029/2019MS001736>, 2019.
- Ge, J., Wang, Z., Liu, Y., Su, J., Wang, C., and Dong, Z.: Linkages between mid-latitude cirrus cloud properties and large-
660 scale meteorology at the SACOL site, *Clim. Dyn.*, 53, 5035-5046, <https://doi.org/10.1007/s00382-019-04843-9>, 2019.
- Hartmann, D. L., Holton, J. R., and Fu, Q.: The heat balance of the tropical tropopause, cirrus, and stratospheric dehydration, *Geophys. Res. Lett.*, 28, 1969-1972, <https://doi.org/10.1029/2000GL012833>, 2001.
- Hersbach, H., Bell, B., Berrisford, P., Hirahara, S., Horányi, A., Muñoz-Sabater, J., Nicolas, J., Peubey, C., Radu, R., Schepers, D., Simmons, A., Soci, C., Abdalla, S., Abellan, X., Balsamo, G., Bechtold, P., Biavati, G., Bidlot, J.,
665 Bonavita, M., De Chiara, G., Dahlgren, P., Dee, D., Diamantakis, M., Dragani, R., Flemming, J., Forbes, R., Fuentes, M., Geer, A., Haimberger, L., Healy, S., Hogan, R. J., Hólm, E., Janisková, M., Keeley, S., Laloyaux, P., Lopez, P., Lupu, C., Radnoti, G., de Rosnay, P., Rozum, I., Vamborg, F., Villaume, S., and Thépaut, J.-N.: The ERA5 global reanalysis, *Q. J. R. Meteorol. Soc.*, 146, 1999-2049, <https://doi.org/10.1002/qj.3803>, 2020.
- Heymsfield, A. J.: Precipitation Development in Stratiform Ice Clouds: A Microphysical and Dynamical Study, *J. Atmos. Sci.*, 34, 367-381, [https://doi.org/10.1175/1520-0469\(1977\)034<0367:Pdisic>2.0.Co;2](https://doi.org/10.1175/1520-0469(1977)034<0367:Pdisic>2.0.Co;2), 1977.
- Heymsfield, A. J., Krämer, M., Luebke, A., Brown, P., Cziczo, D. J., Franklin, C., Lawson, P., Lohmann, U., McFarquhar, G., Ulanowski, Z., and Van Tricht, K.: Cirrus Clouds, *Meteorological Monographs*, 58, 2.1-2.26, <https://doi.org/10.1175/amsmonographs-d-16-0010.1>, 2017.
- Holz, R. E., Ackerman, S. A., Nagle, F. W., Frey, R., Dutcher, S., Kuehn, R. E., Vaughan, M. A., and Baum, B.: Global
675 Moderate Resolution Imaging Spectroradiometer (MODIS) cloud detection and height evaluation using CALIOP, *J. Geophys. Res.-Atmos.*, 113, <https://doi.org/10.1029/2008JD009837>, 2008.



- Igel, M. R., Drager, A. J., and van den Heever, S. C.: A CloudSat cloud object partitioning technique and assessment and integration of deep convective anvil sensitivities to sea surface temperature, *J. Geophys. Res.-Atmos.*, 119, 10515-10535, <https://doi.org/10.1002/2014jd021717>, 2014.
- 680 Imai, T. and Yoshida, R.: Algorithm theoretical basis for Himawari-8 cloud mask product, Meteorological satellite center technical note, 61, 1-17, 2016.
- Karlsson, K.-G. and Devasthale, A.: Inter-Comparison and Evaluation of the Four Longest Satellite-Derived Cloud Climate Data Records: CLARA-A2, ESA Cloud CCI V3, ISCCP-HGM, and PATMOS-x, *Remote Sens.*, 10, 1567, 2018.
- Kirk-Davidoff, D. B., Hintsala, E. J., Anderson, J. G., and Keith, D. W.: The effect of climate change on ozone depletion through changes in stratospheric water vapour, *Nature*, 402, 399-401, <https://doi.org/10.1038/46521>, 1999.
- 685 Kleist, D. T., Parrish, D. F., Derber, J. C., Treadon, R., Wu, W.-S., and Lord, S.: Introduction of the GSI into the NCEPs Global Data Assimilation System, *Wea. Forecasting*, 24, 1691-1705, <https://doi.org/10.1175/2009waf2222201.1>, 2009.
- Kuang, Z. and Bretherton, C. S.: A Mass-Flux Scheme View of a High-Resolution Simulation of a Transition from Shallow to Deep Cumulus Convection, *J. Atmos. Sci.*, 63, 1895-1909, <https://doi.org/10.1175/jas3723.1>, 2006.
- 690 Kukulies, J., Chen, D., and Wang, M.: Temporal and spatial variations of convection and precipitation over the Tibetan Plateau based on recent satellite observations. Part I: Cloud climatology derived from CloudSat and CALIPSO, *Int. J. Climatol.*, 39, 5396-5412, 2019.
- Lei, Y., Letu, H., Shang, H., and Shi, J.: Cloud cover over the Tibetan Plateau and eastern China: a comparison of ERA5 and ERA-Interim with satellite observations, *Clim. Dyn.*, 54, 2941-2957, <https://doi.org/10.1007/s00382-020-05149-x>, 2020.
- 695 Letu, H., Nagao, T. M., Nakajima, T. Y., Riedi, J., Ishimoto, H., Baran, A. J., Shang, H., Sekiguchi, M., and Kikuchi, M.: Ice cloud properties from Himawari-8/AHI next-generation geostationary satellite: Capability of the AHI to monitor the DC cloud generation process, *IEEE Trans. Geosci. Remote Sensing*, 57, 3229-3239, 2018.
- Letu, H., Yang, K., Nakajima, T. Y., Ishimoto, H., Nagao, T. M., Riedi, J., Baran, A. J., Ma, R., Wang, T., and Shang, H.: High-resolution retrieval of cloud microphysical properties and surface solar radiation using Himawari-8/AHI next-generation geostationary satellite, *Remote Sens. of Environment*, 239, 111583, 2020.
- 700 Li, J., Mao, J., and Wang, F.: Comparative study of five current reanalyses in characterizing total cloud fraction and top-of-the-atmosphere cloud radiative effects over the Asian monsoon region, *Int. J. Climatol.*, 37, 5047-5067, <https://doi.org/10.1002/joc.5143>, 2017.
- Li, J., Jian, B., Zhao, C., Zhao, Y., Wang, J., and Huang, J.: Atmospheric Instability Dominates the Long-Term Variation of Cloud Vertical Overlap Over the Southern Great Plains Site, *J. Geophys. Res.-Atmos.*, 124, 9691-9701, <https://doi.org/10.1029/2019JD030954>, 2019.
- 705 Li, J., Lv, Q., Jian, B., Zhang, M., Zhao, C., Fu, Q., Kawamoto, K., and Zhang, H.: The impact of atmospheric stability and wind shear on vertical cloud overlap over the Tibetan Plateau, *Atmos. Chem. Phys.*, 18, 7329-7343, <https://doi.org/10.5194/acp-18-7329-2018>, 2018.



- 710 Li, J., Yi, Y., Minnis, P., Huang, J., Yan, H., Ma, Y., Wang, W., and Kirk Ayers, J.: Radiative effect differences between multi-layered and single-layer clouds derived from CERES, CALIPSO, and CloudSat data, *J. Quant. Spectrosc. Radiat. Transf.*, 112, 361-375, <https://doi.org/10.1016/j.jqsrt.2010.10.006>, 2011.
- Li, Y. and Zhang, M.: Cumulus over the Tibetan Plateau in the Summer Based on CloudSat–CALIPSO Data, *J. Clim.*, 29, 1219-1230, <https://doi.org/10.1175/jcli-d-15-0492.1>, 2016.
- 715 Liou, K.-N.: Influence of Cirrus Clouds on Weather and Climate Processes: A Global Perspective, *Mon. Weather Rev.*, 114, 1167-1199, [https://doi.org/10.1175/1520-0493\(1986\)114<1167:Ioccow>2.0.Co;2](https://doi.org/10.1175/1520-0493(1986)114<1167:Ioccow>2.0.Co;2), 1986.
- Liu, L., Zheng, J., Ruan, Z., Cui, Z., Hu, Z., Wu, S., Dai, G., and Wu, Y.: Comprehensive radar observations of clouds and precipitation over the Tibetan Plateau and preliminary analysis of cloud properties, *J. Meteorol. Res.*, 29, 546-561, <https://doi.org/10.1007/s13351-015-4208-6>, 2015.
- 720 Liu, X. and Chen, B.: Climatic warming in the Tibetan Plateau during recent decades, *Int. J. Climatol.*, 20, 1729-1742, [https://doi.org/10.1002/1097-0088\(20001130\)20:14<1729::AID-JOC556>3.0.CO;2-Y](https://doi.org/10.1002/1097-0088(20001130)20:14<1729::AID-JOC556>3.0.CO;2-Y), 2000.
- Luo, Y., Zhang, R., Qian, W., Luo, Z., and Hu, X.: Intercomparison of Deep Convection over the Tibetan Plateau–Asian Monsoon Region and Subtropical North America in Boreal Summer Using CloudSat/CALIPSO Data, *J. Clim.*, 24, 2164-2177, <https://doi.org/10.1175/2010JCLI4032.1>, 2011.
- 725 Ma, Q., You, Q., Ma, Y., Cao, Y., Zhang, J., Niu, M., and Zhang, Y.: Changes in cloud amount over the Tibetan Plateau and impacts of large-scale circulation, *Atmos. Res.*, 249, 105332, <https://doi.org/10.1016/j.atmosres.2020.105332>, 2021.
- Ma, Z., Liu, Q., Zhao, C., Shen, X., Wang, Y., Jiang, J. H., Li, Z., and Yung, Y.: Application and Evaluation of an Explicit Prognostic Cloud-Cover Scheme in GRAPES Global Forecast System, *J. Adv. Model. Earth Syst.*, 10, 652-667, <https://doi.org/10.1002/2017MS001234>, 2018.
- 730 Mace, G. G., Benson, S., and Vernon, E.: Cirrus Clouds and the Large-Scale Atmospheric State: Relationships Revealed by Six Years of Ground-Based Data, *J. Clim.*, 19, 3257-3278, <https://doi.org/10.1175/jcli3786.1>, 2006.
- Marchand, R., Ackerman, T., Smyth, M., and Rossow, W. B.: A review of cloud top height and optical depth histograms from MISR, ISCCP, and MODIS, *J. Geophys. Res.-Atmos.*, 115, <https://doi.org/10.1029/2009JD013422>, 2010.
- Matsui, T., Masunaga, H., Kreidenweis, S. M., Pielke Sr., R. A., Tao, W.-K., Chin, M., and Kaufman, Y. J.: Satellite-based
735 assessment of marine low cloud variability associated with aerosol, atmospheric stability, and the diurnal cycle, *J. Geophys. Res.-Atmos.*, 111, <https://doi.org/10.1029/2005JD006097>, 2006.
- McGill, M. J., Yorks, J. E., Scott, V. S., Kupchock, A. W., and Selmer, P. A.: The Cloud-Aerosol Transport System (CATS): a technology demonstration on the International Space Station, proceedings of spie, 9612, 34-39, <https://doi.org/10.1117/12.2190841>, 2015.
- 740 Miao, H., Wang, X., Liu, Y., and Wu, G.: An evaluation of cloud vertical structure in three reanalyses against CloudSat/cloud-aerosol lidar and infrared pathfinder satellite observations, *Atmos. Sci. Lett.*, 20, e906, <https://doi.org/10.1002/asl.906>, 2019.



- Minnis, P., Trepte, Q. Z., Sun-Mack, S., Chen, Y., Doelling, D. R., Young, D. F., Spangenberg, D. A., Miller, W. F., Wielicki, B. A., Brown, R. R., Gibson, S. C., and Geier, E. B.: Cloud Detection in Nonpolar Regions for CERES Using TRMM VIRS and Terra and Aqua MODIS Data, *IEEE Trans. Geosci. Remote Sensing*, 46, 3857-3884, <https://doi.org/10.1109/TGRS.2008.2001351>, 2008.
- 745
- Molod, A.: Constraints on the Profiles of Total Water PDF in AGCMs from AIRS and a High-Resolution Model, *J. Clim.*, 25, 8341-8352, <https://doi.org/10.1175/jcli-d-11-00412.1>, 2012.
- Molod, A., Takacs, L., Suárez, M., and Bacmeister, J.: Development of the GEOS-5 atmospheric general circulation model: Evolution from MERRA to MERRA2, *Geosci. Model Dev.*, 8, 1339-1356, <https://doi.org/10.5194/gmd-8-1339-2015>, 2015.
- 750
- Naud, C. M. and Chen, Y.-H.: Assessment of ISCCP cloudiness over the Tibetan Plateau using CloudSat-CALIPSO, *J. Geophys. Res.-Atmos.*, 115, <https://doi.org/10.1029/2009JD013053>, 2010.
- Naud, C. M., Rangwala, I., Xu, M., and Miller, J. R.: A Satellite View of the Radiative Impact of Clouds on Surface Downward Fluxes in the Tibetan Plateau, *J. Appl. Meteorol. Climatol.*, 54, 479-493, <https://doi.org/10.1175/JAMC-D-14-0183.1>, 2015.
- 755
- Nesbitt, S. W., Gochis, D. J., and Lang, T. J.: The Diurnal Cycle of Clouds and Precipitation along the Sierra Madre Occidental Observed during NAME-2004: Implications for Warm Season Precipitation Estimation in Complex Terrain, *J. Hydrometeorol.*, 9, 728-743, <https://doi.org/10.1175/2008jhm939.1>, 2008.
- 760
- Noel, V., Chepfer, H., Chiriaco, M., and Yorks, J.: The diurnal cycle of cloud profiles over land and ocean between 51°S and 51°N, seen by the CATS spaceborne lidar from the International Space Station, *Atmos. Chem. Phys.*, 18, 9457-9473, <https://doi.org/10.5194/acp-18-9457-2018>, 2018.
- Norris, J. R. and Evan, A. T.: Empirical Removal of Artifacts from the ISCCP and PATMOS-x Satellite Cloud Records, *J. Atmos. Ocean. Technol.*, 32, 691-702, <https://doi.org/10.1175/jtech-d-14-00058.1>, 2015.
- 765
- Ntwali, D. and Chen, H.: Diurnal spatial distributions of aerosol optical and cloud micro-macrophysics properties in Africa based on MODIS observations, *Atmos. Environ.*, 182, 252-262, <https://doi.org/10.1016/j.atmosenv.2018.03.054>, 2018.
- Oreopoulos, L., Cho, N., and Lee, D.: New insights about cloud vertical structure from CloudSat and CALIPSO observations, *J. Geophys. Res.-Atmos.*, 122, 9280-9300, <https://doi.org/10.1002/2017JD026629>, 2017.
- Pan, Z., Mao, F., Gong, W., Min, Q., and Wang, W.: The warming of Tibetan Plateau enhanced by 3D variation of low-level clouds during daytime, *Remote Sens. Environ.*, 198, 363-368, <https://doi.org/10.1016/j.rse.2017.06.024>, 2017.
- 770
- Pauly, R. M., Yorks, J. E., Hlavka, D. L., McGill, M. J., Amiridis, V., Palm, S. P., Rodier, S. D., Vaughan, M. A., Selmer, P. A., Kupchok, A. W., Baars, H., and Gialitaki, A.: Cloud-Aerosol Transport System (CATS) 1064 nm calibration and validation, *Atmos. Meas. Tech.*, 12, 6241-6258, <https://doi.org/10.5194/amt-12-6241-2019>, 2019.
- Posselt, D. J., Stephens, G. L., and Miller, M.: CLOUDSAT: Adding a New Dimension to a Classical View of Extratropical Cyclones, *Bull. Amer. Meteorol. Soc.*, 89, 599-610, <https://doi.org/10.1175/bams-89-5-599>, 2008.
- 775



- Rajapakshe, C., Zhang, Z., Yorks, J. E., Yu, H., Tan, Q., Meyer, K., Platnick, S., and Winker, D. M.: Seasonally transported aerosol layers over southeast Atlantic are closer to underlying clouds than previously reported, *Geophys. Res. Lett.*, 44, 5818-5825, <https://doi.org/10.1002/2017GL073559>, 2017.
- Ramaswamy, V. and Detwiler, A.: Interdependence of radiation and microphysics in cirrus clouds, *J. Atmos. Sci.*, 43, 2289-2301, [https://doi.org/10.1175/1520-0469\(1986\)043<2289:Iorami>2.0.Co;2](https://doi.org/10.1175/1520-0469(1986)043<2289:Iorami>2.0.Co;2), 1986.
- 780
- Rangwala, I., Miller, J. R., and Xu, M.: Warming in the Tibetan Plateau: Possible influences of the changes in surface water vapor, *Geophys. Res. Lett.*, 36, <https://doi.org/10.1029/2009GL037245>, 2009.
- Rangwala, I., Miller, J. R., Russell, G. L., and Xu, M.: Using a global climate model to evaluate the influences of water vapor, snow cover and atmospheric aerosol on warming in the Tibetan Plateau during the twenty-first century, *Clim. Dyn.*, 34, 859-872, <https://doi.org/10.1007/s00382-009-0564-1>, 2010.
- 785
- Rienecker, M. M.: The GEOS-5 Data Assimilation System—Documentation of versions 5.0.1, 5.1.0, and 5.2.0. Technical Report Series on Global Modeling and Data Assimilation, NASA Technical Reports 27, 118, Available online at <https://gmao.gsfc.nasa.gov/pubs/docs/Rienecker369.pdf>, 2008.
- Rienecker, M. M., Suarez, M. J., Gelaro, R., Todling, R., Bacmeister, J., Liu, E., Bosilovich, M. G., Schubert, S. D., Takacs, L., Kim, G.-K., Bloom, S., Chen, J., Collins, D., Conaty, A., da Silva, A., Gu, W., Joiner, J., Koster, R. D., Lucchesi, R., Molod, A., Owens, T., Pawson, S., Pegion, P., Redder, C. R., Reichle, R., Robertson, F. R., Ruddick, A. G., Sienkiewicz, M., and Woollen, J.: MERRA: NASA's Modern-Era Retrospective Analysis for Research and Applications, *J. Clim.*, 24, 3624-3648, <https://doi.org/10.1175/jcli-d-11-00015.1>, 2011.
- 790
- Rossow, W. B. and Schiffer, R. A.: Advances in Understanding Clouds from ISCCP, *Bull. Amer. Meteorol. Soc.*, 80, 2261-2288, [https://doi.org/10.1175/1520-0477\(1999\)080<2261:Aiucfi>2.0.Co;2](https://doi.org/10.1175/1520-0477(1999)080<2261:Aiucfi>2.0.Co;2), 1999.
- Rossow, W. B., Knapp, K. R., and Young, A. H.: International Satellite Cloud Climatology Project: Extending the Record, *J. Clim.*, 1-62, <https://doi.org/10.1175/jcli-d-21-0157.1>, 2021.
- Sassen, K. and Benson, S.: A midlatitude cirrus cloud climatology from the facility for atmospheric remote sensing. Part II: Microphysical properties derived from lidar depolarization, *J. Atmos. Sci.*, 58, 2103-2112, [https://doi.org/10.1175/1520-0469\(2001\)058<2103:AMCCCF>2.0.CO;2](https://doi.org/10.1175/1520-0469(2001)058<2103:AMCCCF>2.0.CO;2), 2001.
- 800
- Sassen, K. and Cho, B. S.: Subvisual-Thin Cirrus Lidar Dataset for Satellite Verification and Climatological Research, *J. Appl. Meteorol. Climatol.*, 31, 1275-1285, [https://doi.org/10.1175/1520-0450\(1992\)031<1275:Stcldf>2.0.Co;2](https://doi.org/10.1175/1520-0450(1992)031<1275:Stcldf>2.0.Co;2), 1992.
- Sassen, K., Starr, D. O. C., and Uttal, T.: Mesoscale and Microscale Structure of Cirrus Clouds: Three Case Studies, *J. Atmos. Sci.*, 46, 371-396, [https://doi.org/10.1175/1520-0469\(1989\)046<0371:Mamsoc>2.0.Co;2](https://doi.org/10.1175/1520-0469(1989)046<0371:Mamsoc>2.0.Co;2), 1989.
- 805
- Sassen, K., Wang, Z., and Liu, D.: Cirrus clouds and deep convection in the tropics: Insights from CALIPSO and CloudSat, *J. Geophys. Res.-Atmos.*, 114, <https://doi.org/10.1029/2009JD011916>, 2009.
- Shang, H., Letu, H., Nakajima, T. Y., Wang, Z., Ma, R., Wang, T., Lei, Y., Ji, D., Li, S., and Shi, J.: Diurnal cycle and seasonal variation of cloud cover over the Tibetan Plateau as determined from Himawari-8 new-generation geostationary satellite data, *Sci. Rep.*, 8, 1105, <https://doi.org/10.1038/s41598-018-19431-w>, 2018.



- 810 Song, X., Zhai, X., Liu, L., and Wu, S.: Lidar and Ceilometer Observations and Comparisons of Atmospheric Cloud Structure at Nagqu of Tibetan Plateau in 2014 Summer, *Atmosphere*, 8, 9, 2017.
- Stanfield, R. E., Dong, X., Xi, B., Del Genio, A. D., Minnis, P., Doelling, D., and Loeb, N.: Assessment of NASA GISS CMIP5 and Post-CMIP5 Simulated Clouds and TOA Radiation Budgets Using Satellite Observations. Part II: TOA Radiation Budget and CREs, *J. Clim.*, 28, 1842, <https://doi.org/10.1175/jcli-d-14-00249.1>, 2015.
- 815 Sun, W., Videen, G., and Mishchenko, M. I.: Detecting super-thin clouds with polarized sunlight, *Geophys. Res. Lett.*, 41, 688-693, <https://doi.org/10.1002/2013GL058840>, 2014.
- Sun, W., Baize, R. R., Videen, G., Hu, Y., and Fu, Q.: A method to retrieve super-thin cloud optical depth over ocean background with polarized sunlight, *Atmos. Chem. Phys.*, 15, 11909-11918, <https://doi.org/10.5194/acp-15-11909-2015>, 2015.
- 820 Sun, W., Videen, G., Kato, S., Lin, B., Lukashin, C., and Hu, Y.: A study of subvisual clouds and their radiation effect with a synergy of CERES, MODIS, CALIPSO, and AIRS data, *J. Geophys. Res.-Atmos.*, 116, <https://doi.org/10.1029/2011JD016422>, 2011a.
- Sun, W. B., Lin, B., Hu, Y. X., Lukashin, C., Kato, S., and Liu, Z. Y.: On the consistency of CERES longwave flux and AIRS temperature and humidity profiles, *J. Geophys. Res.-Atmos.*, 116, <https://doi.org/10.1029/2011JD016153>, 2011b.
- 825 Taylor, K. E.: Summarizing multiple aspects of model performance in a single diagram, *J. Geophys. Res.-Atmos.*, 106, 7183-7192, <https://doi.org/10.1029/2000JD900719>, 2001.
- Tian, B., Soden, B. J., and Wu, X.: Diurnal cycle of convection, clouds, and water vapor in the tropical upper troposphere: Satellites versus a general circulation model, *J. Geophys. Res.-Atmos.*, 109, <https://doi.org/10.1029/2003JD004117>, 2004.
- 830 Tian, H., Xu, X., Chen, H., Huang, R., Zhang, S., and Luo, J.: Analysis of the Anomalous Signals near the Tropopause before the Overshooting Convective System Onset over the Tibetan Plateau, *Adv. Meteorol.*, 2020, 8823446, <https://doi.org/10.1155/2020/8823446>, 2020.
- Tian, W., Tian, H., Dhomse, S., and Feng, W.: A study of upper troposphere and lower stratosphere water vapor above the Tibetan Plateau using AIRS and MLS data, *Atmos. Sci. Lett.*, 12, 233-239, <https://doi.org/10.1002/asl.319>, 2011.
- 835 Tiedtke, M.: Representation of Clouds in Large-Scale Models, *Mon. Weather Rev.*, 121, 3040-3061, [https://doi.org/10.1175/1520-0493\(1993\)121<3040:Rocils>2.0.Co;2](https://doi.org/10.1175/1520-0493(1993)121<3040:Rocils>2.0.Co;2), 1993.
- Tselioudis, G., Rossow, W. B., Jakob, C., Remillard, J., Tropf, D., and Zhang, Y.: Evaluation of Clouds, Radiation, and Precipitation in CMIP6 Models Using Global Weather States Derived from ISCCP-H Cloud Property Data, *J. Clim.*, 34, 7311-7324, <https://doi.org/10.1175/jcli-d-21-0076.1>, 2021.
- 840 Tzallas, V., Hatzianastassiou, N., Benas, N., Meirink, J. F., Matsoukas, C., Stackhouse, P., and Vardavas, I.: Evaluation of CLARA-A2 and ISCCP-H Cloud Cover Climate Data Records over Europe with ECA&D Ground-Based Measurements, *Remote Sens.*, 11, 212, 2019.



- Urraca, R., Huld, T., Gracia-Amillo, A., Martinez-de-Pison, F. J., Kaspar, F., and Sanz-Garcia, A.: Evaluation of global horizontal irradiance estimates from ERA5 and COSMO-REA6 reanalyses using ground and satellite-based data, *Sol. Energy*, 164, 339-354, <https://doi.org/10.1016/j.solener.2018.02.059>, 2018.
- 845 Vignesh, P. P., Jiang, J. H., Kishore, P., Su, H., Smay, T., Brighton, N., and Velicogna, I.: Assessment of CMIP6 Cloud Fraction and Comparison with Satellite Observations, *Earth Space Sci.*, 7, e2019EA000975, <https://doi.org/10.1029/2019EA000975>, 2020.
- Virts, K. S., Wallace, J. M., Fu, Q., and Ackerman, T. P.: Tropical Tropopause Transition Layer Cirrus as Represented by CALIPSO Lidar Observations, *J. Atmos. Sci.*, 67, 3113-3129, <https://doi.org/10.1175/2010jas3412.1>, 2010.
- 850 Wang, B., Bao, Q., Hoskins, B., Wu, G., and Liu, Y.: Tibetan Plateau warming and precipitation changes in East Asia, *Geophys. Res. Lett.*, 35, <https://doi.org/10.1029/2008GL034330>, 2008.
- Wang, J. and Rossow, W. B.: Determination of Cloud Vertical Structure from Upper-Air Observations, *J. Appl. Meteorol. Climatol.*, 34, 2243-2258, [https://doi.org/10.1175/1520-0450\(1995\)034<2243:Docvsf>2.0.Co;2](https://doi.org/10.1175/1520-0450(1995)034<2243:Docvsf>2.0.Co;2), 1995.
- 855 Wang, J., Rossow, W. B., and Zhang, Y.: Cloud Vertical Structure and Its Variations from a 20-Yr Global Rawinsonde Dataset, *J. Clim.*, 13, 3041-3056, [https://doi.org/10.1175/1520-0442\(2000\)013<3041:Cvsai>2.0.Co;2](https://doi.org/10.1175/1520-0442(2000)013<3041:Cvsai>2.0.Co;2), 2000.
- Wang, J., Jian, B., Wang, G., Zhao, Y., Li, Y., Letu, H., Zhang, M., and Li, J.: Climatology of Cloud Phase, Cloud Radiative Effects and Precipitation Properties over the Tibetan Plateau, *Remote Sens.*, 13, 363, 2021.
- Wang, Y., Li, J., Zhao, Y., Li, Y., Zhao, Y., and Wu, X.: Distinct Diurnal Cycle of Supercooled Water Cloud Fraction Dominated by Dust Extinction Coefficient, *Geophys. Res. Lett.*, 49, e2021GL097006, <https://doi.org/10.1029/2021GL097006>, 2022.
- 860 Wang, Y., Zeng, X., Xu, X., Welty, J., Lenschow, D. H., Zhou, M., and Zhao, Y.: Why Are There More Summer Afternoon Low Clouds Over the Tibetan Plateau Compared to Eastern China?, *Geophys. Res. Lett.*, 47, e2020GL089665, <https://doi.org/10.1029/2020GL089665>, 2020.
- 865 Wu, G., He, B., Duan, A., Liu, Y., and Yu, W.: Formation and variation of the atmospheric heat source over the Tibetan Plateau and its climate effects, *Adv. Atmos. Sci.*, 34, 1169-1184, <https://doi.org/10.1007/s00376-017-7014-5>, 2017.
- Wu, G., Liu, Y., He, B., Bao, Q., Duan, A., and Jin, F.-F.: Thermal Controls on the Asian Summer Monsoon, *Sci. Rep.*, 2, 404, <https://doi.org/10.1038/srep00404>, 2012.
- Wu, W.-S., Purser, R. J., and Parrish, D. F.: Three-dimensional variational analysis with spatially inhomogeneous covariances, *Mon. Wea. Rev.*, 130, 2905-2916, [https://doi.org/10.1175/1520-0493\(2002\)130<2905:Tdvaws>2.0.Co;2](https://doi.org/10.1175/1520-0493(2002)130<2905:Tdvaws>2.0.Co;2), 2002.
- 870 Xiaoduo, P. A. N., Huixia, R. E. N., and Yili, Z.: Integration dataset of Tibet Plateau boundary, National Tibetan Plateau Data Center, <https://doi.org/10.11888/Geogra.tpdc.270099>, 2019.
- Xu, X., Lu, C., Shi, X., and Gao, S.: World water tower: An atmospheric perspective, *Geophys. Res. Lett.*, 35, <https://doi.org/10.1029/2008GL035867>, 2008.
- 875



- Xu, X., Xiaohui Shi, and Chungu Lu: Theory and Application for Warning and Prediction of Disastrous Weather Downstream from the Tibetan Plateau, Novinka Science Publishers, Inc. New York, 2012.
- Yan, Y., Liu, Y., and Lu, J.: Cloud vertical structure, precipitation, and cloud radiative effects over Tibetan Plateau and its neighboring regions, *J. Geophys. Res.-Atmos.*, 121, 5864-5877, <https://doi.org/10.1002/2015JD024591>, 2016.
- 880 Yang, J., Hu, X., Lei, H., Duan, Y., Lv, F., and Zhao, L.: Airborne Observations of Microphysical Characteristics of Stratiform Cloud Over Eastern Side of Taihang Mountains, *Chinese J. Atmos. Sci.*, 45, 88, <https://doi.org/10.3878/j.issn.1006-9895.2004.19202>, 2021.
- Yang, K., Ding, B., Qin, J., Tang, W., Lu, N., and Lin, C.: Can aerosol loading explain the solar dimming over the Tibetan Plateau, *Geophys. Res. Lett.*, 39, <https://doi.org/10.1029/2012GL053733>, 2012.
- 885 Yao, T., Pu, J., Lu, A., Wang, Y., and Yu, W.: Recent Glacial Retreat and Its Impact on Hydrological Processes on the Tibetan Plateau, China, and Surrounding Regions, *Arct. Antarct. Alp. Res.*, 39, 642-650, [https://doi.org/10.1657/1523-0430\(07-510\)\[YAO\]2.0.CO;2](https://doi.org/10.1657/1523-0430(07-510)[YAO]2.0.CO;2), 2007.
- Yao, T., Masson-Delmotte, V., Gao, J., Yu, W., Yang, X., Risi, C., Sturm, C., Werner, M., Zhao, H., and He, Y.: A review of climatic controls on $\delta^{18}\text{O}$ in precipitation over the Tibetan Plateau: Observations and simulations, *Rev. Geophys.*, 51, 890 525-548, 2013.
- Yao, T., Thompson, L., Yang, W., Yu, W., Gao, Y., Guo, X., Yang, X., Duan, K., Zhao, H., Xu, B., Pu, J., Lu, A., Xiang, Y., Kattel, D. B., and Joswiak, D.: Different glacier status with atmospheric circulations in Tibetan Plateau and surroundings, *Nat. Clim. Chang.*, 2, 663-667, <https://doi.org/10.1038/NCLIMATE1580>, 2012.
- Yeo, H., Kim, M.-H., Son, S.-W., Jeong, J.-H., Yoon, J.-H., Kim, B.-M., and Kim, S.-W.: Arctic cloud properties and associated radiative effects in the three newer reanalysis datasets (ERA5, MERRA-2, JRA-55): Discrepancies and 895 possible causes, *Atmos. Res.*, 270, 106080, <https://doi.org/10.1016/j.atmosres.2022.106080>, 2022.
- Yin, J. and Porporato, A.: Diurnal cloud cycle biases in climate models, *Nat. Commun.*, 8, 2269, <https://doi.org/10.1038/s41467-017-02369-4>, 2017.
- Yin, J. and Porporato, A.: Radiative effects of daily cycle of cloud frequency in past and future climates, *Clim. Dyn.*, 54, 900 1625-1637, <https://doi.org/10.1007/s00382-019-05077-5>, 2020.
- Yin, J., Wang, D., Xu, H., and Zhai, G.: An investigation into the three-dimensional cloud structure over East Asia from the CALIPSO-GOCCP Data, *Sci. China-Earth Sci.*, 58, 2236-2248, <https://doi.org/10.1007/s11430-015-5205-4>, 2015.
- Yorks, J. E., Selmer, P. A., Kupchock, A., Nowottnick, E. P., Christian, K. E., Rusinek, D., Dacic, N., and McGill, M. J.: Aerosol and Cloud Detection Using Machine Learning Algorithms and Space-Based Lidar Data, *Atmosphere*, 12, 606, 905 2021.
- Yorks, J. E., McGill, M. J., Palm, S. P., Hlavka, D. L., Selmer, P. A., Nowottnick, E. P., Vaughan, M. A., Rodier, S. D., and Hart, W. D.: An overview of the CATS level 1 processing algorithms and data products, *Geophys. Res. Lett.*, 43, 4632-4639, <https://doi.org/10.1002/2016GL068006>, 2016.



- 910 You, Q., Jiao, Y., Lin, H., Min, J., Kang, S., Ren, G., and Meng, X.: Comparison of NCEP/NCAR and ERA-40 total cloud cover with surface observations over the Tibetan Plateau, *Int. J. Climatol.*, 34, 2529-2537, <https://doi.org/10.1002/joc.3852>, 2014.
- Young, A. H., Knapp, K. R., Inamdar, A., Hankins, W., and Rossow, W. B.: The International Satellite Cloud Climatology Project H-Series climate data record product, *Earth Syst. Sci. Data*, 10, 583-593, <https://doi.org/10.5194/essd-10-583-2018>, 2018.
- 915 Yu, Y., Kalashnikova, O. V., Garay, M. J., Lee, H., Choi, M., Okin, G. S., Yorks, J. E., Campbell, J. R., and Marquis, J.: A global analysis of diurnal variability in dust and dust mixture using CATS observations, *Atmos. Chem. Phys.*, 21, 1427-1447, <https://doi.org/10.5194/acp-21-1427-2021>, 2021.
- Zhang, F., Yu, Q. R., Mao, J. L., Dan, C., Wang, Y., He, Q., Cheng, T., Chen, C., Liu, D., and Gao, Y.: Possible mechanisms of summer cirrus clouds over the Tibetan Plateau, *Atmos. Chem. Phys.*, 20, 11799-11808, <https://doi.org/10.5194/acp-20-11799-2020>, 2020a.
- 920 Zhang, G., Chen, W., and Xie, H.: Tibetan Plateau's Lake Level and Volume Changes from NASA's ICESat/ICESat-2 and Landsat Missions, *Geophys. Res. Lett.*, 46, 13107-13118, <https://doi.org/10.1029/2019GL085032>, 2019.
- Zhang, L., Lau, W., Tao, W., and Li, Z.: Large Wildfires in the Western United States Exacerbated by Tropospheric Drying Linked to a Multi-Decadal Trend in the Expansion of the Hadley Circulation, *Geophys. Res. Lett.*, 47, e2020GL087911, <https://doi.org/10.1029/2020GL087911>, 2020b.
- 925 Zhao, W., Marchand, R., and Fu, Q.: The diurnal cycle of clouds and precipitation at the ARM SGP site: Cloud radar observations and simulations from the multiscale modeling framework, *J. Geophys. Res.-Atmos.*, 122, 7519-7536, <https://doi.org/10.1002/2016JD026353>, 2017.
- Zhou, R., Wang, G., and Zhaxi, S.: Cloud vertical structure measurements from a ground-based cloud radar over the southeastern Tibetan Plateau, *Atmos. Res.*, 258, 105629, <https://doi.org/10.1016/j.atmosres.2021.105629>, 2021.
- 930 Zhou, T. J. and Zhang, W. X.: Anthropogenic warming of Tibetan Plateau and constrained future projection, *Environ. Res. Lett.*, 16, <https://doi.org/10.1088/1748-9326/abede8>, 2021.
- Zou, L., Griessbach, S., Hoffmann, L., Gong, B., and Wang, L.: Revisiting global satellite observations of stratospheric cirrus clouds, *Atmos. Chem. Phys.*, 20, 9939-9959, <https://doi.org/10.5194/acp-20-9939-2020>, 2020.
- 935 Zou, L., Hoffmann, L., Griessbach, S., Spang, R., and Wang, L.: Empirical evidence for deep convection being a major source of stratospheric ice clouds over North America, *Atmos. Chem. Phys.*, 21, 10457-10475, <https://doi.org/10.5194/acp-21-10457-2021>, 2021.

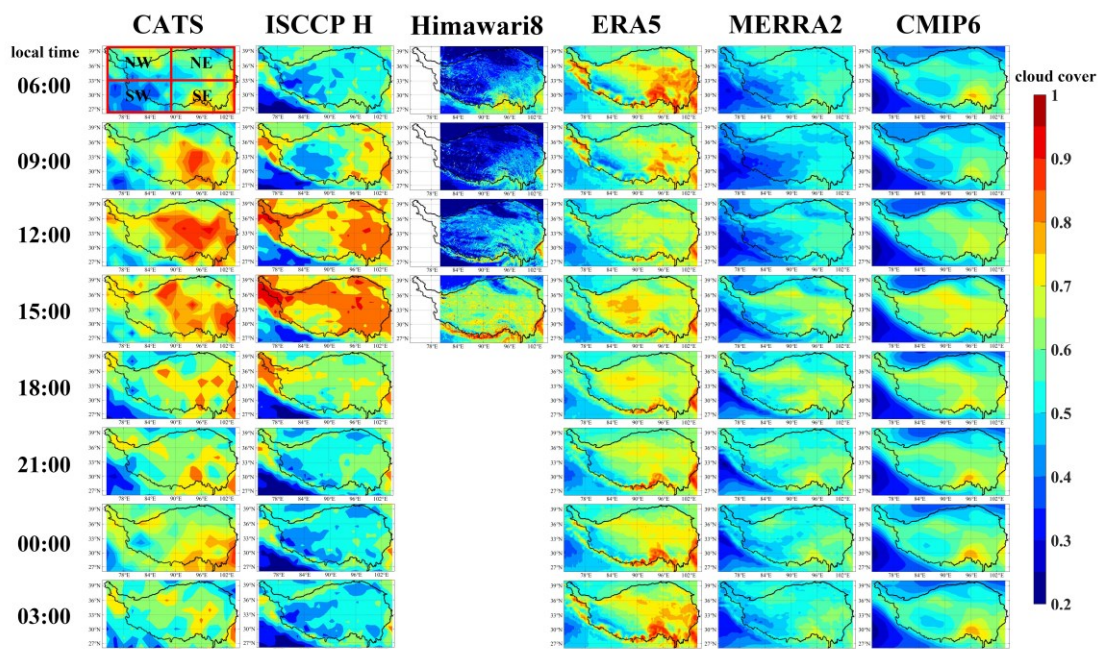


Data	Temporal Coverage	Spatial Resolution	Temporal Resolution
CATS	2015.3.26-2017.10.29	orbital profiles	orbital profiles
ISCCP	2015.3-2017.6	1° × 1°	3 hours
Himawari-8	2016.1.1-2017.10.29	0.05° × 0.05°	10 min
ERA5	2015.3.26-2017.10.29	0.25° × 0.25°	1 hour
MERRA2	2015.3.26-2017.10.29	0.5° × 0.625°	1 hour for single level/3 hours for pressure level

The CMIP6 model names and their horizontal resolutions

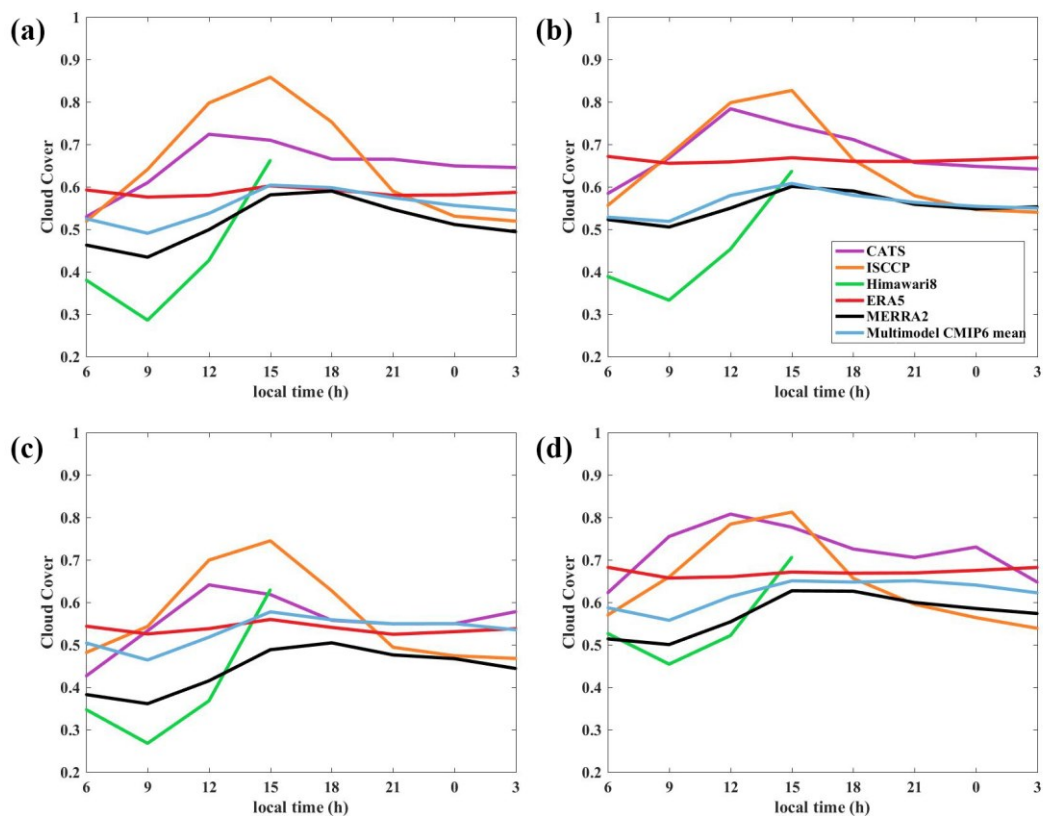
No	Source ID	Resolution	Temporal Resolution
1	BCC-CSM2-MR	160×320	3 hours
2	EC-Earth3	256×512	3 hours
3	EC-Earth3-Veg	256×512	3 hours
4	FGOALS-f3	180×288	3 hours
5	FGOALS-g3	80×180	3 hours
6	IPSL-CM6A-LR	143×144	3 hours
7	KACE-1-0	144×192	3 hours
8	MIROC6	128×256	3 hours
9	MRI-ESM2-0	160×320	3 hours
10	MPI-ESMI-2-HR	192×384	3 hours
11	NESM3	96×192	3 hours
12	SAM0-UNICON	192×288	3 hours

Table 1: The temporal coverage and resolution of datasets used in this study. The temporal coverage of all CMIP6 model outputs is from 1979 to 2014.

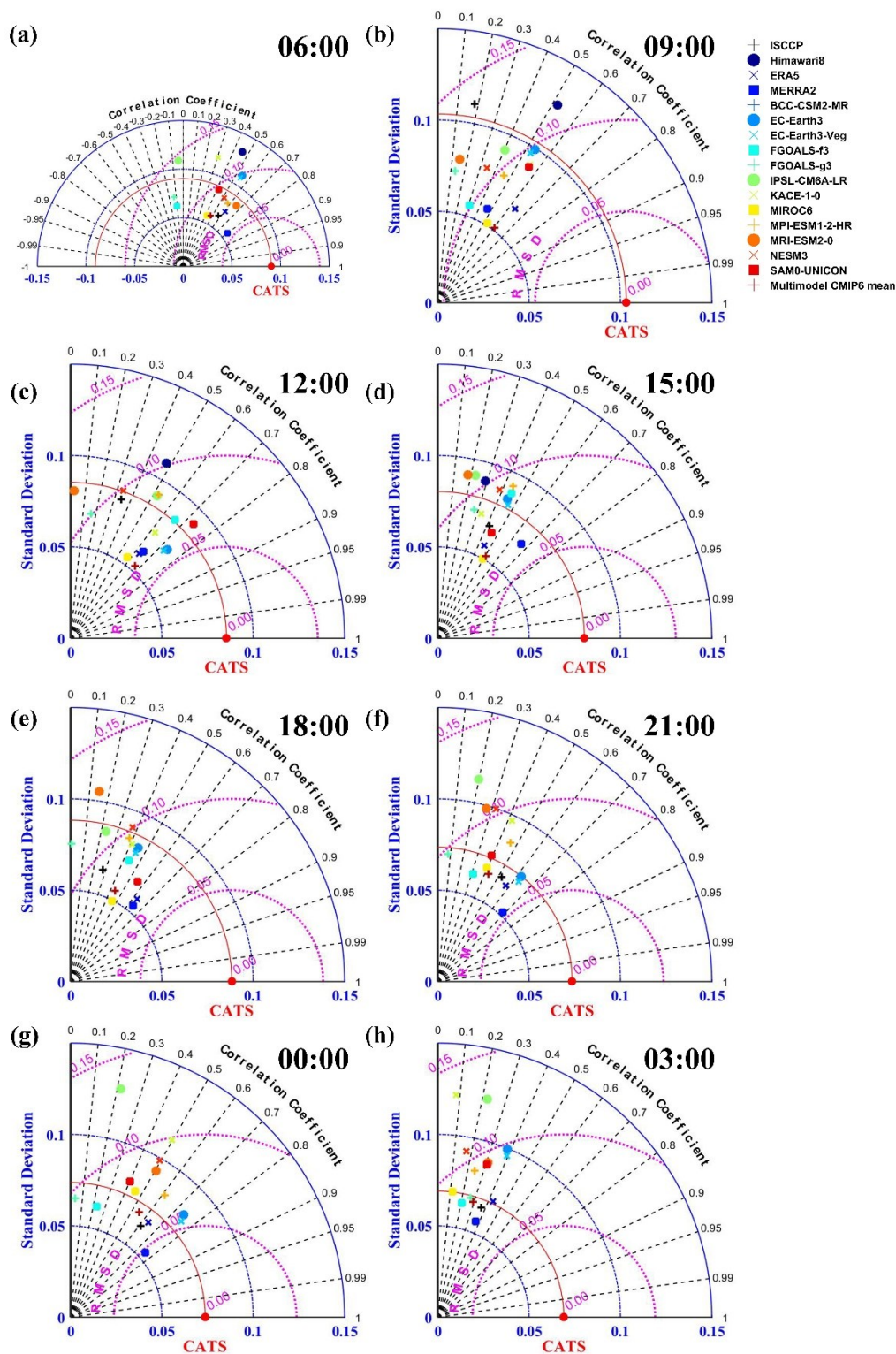


945

Figure 1: The spatial distribution of 3-hourly averaged total cloud cover over the TP based on CATS, ISCCP-H, Himawari-8, ERA5, MERRA-2, CMIP6 multimodel mean. The different TP regions involved in the following part of this study are shown in the upper-left image.

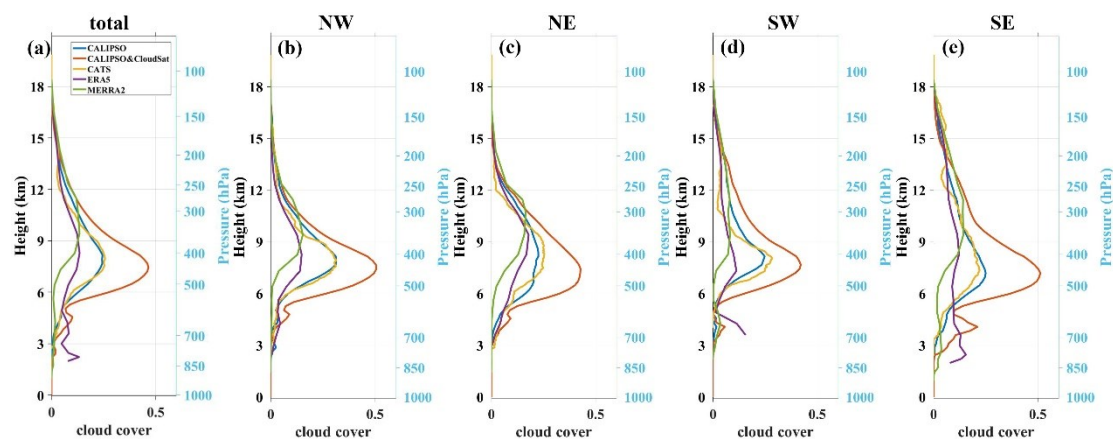


950 **Figure 2:** The 3-hourly mean total cloud cover in different regions of TP based on CATS (purple lines), ISCCP-H (orange lines), Himawari-8 (green lines), ERA5 (red lines), MERRA-2 (black lines), CMIP6 multimodel mean (blue lines). (a) The northwestern TP (b) The northeastern TP (c) The southwestern TP (d) The southeastern TP. The regions are divided by latitude and longitude lines of 33°N and 89°E (shown in Fig. 1).

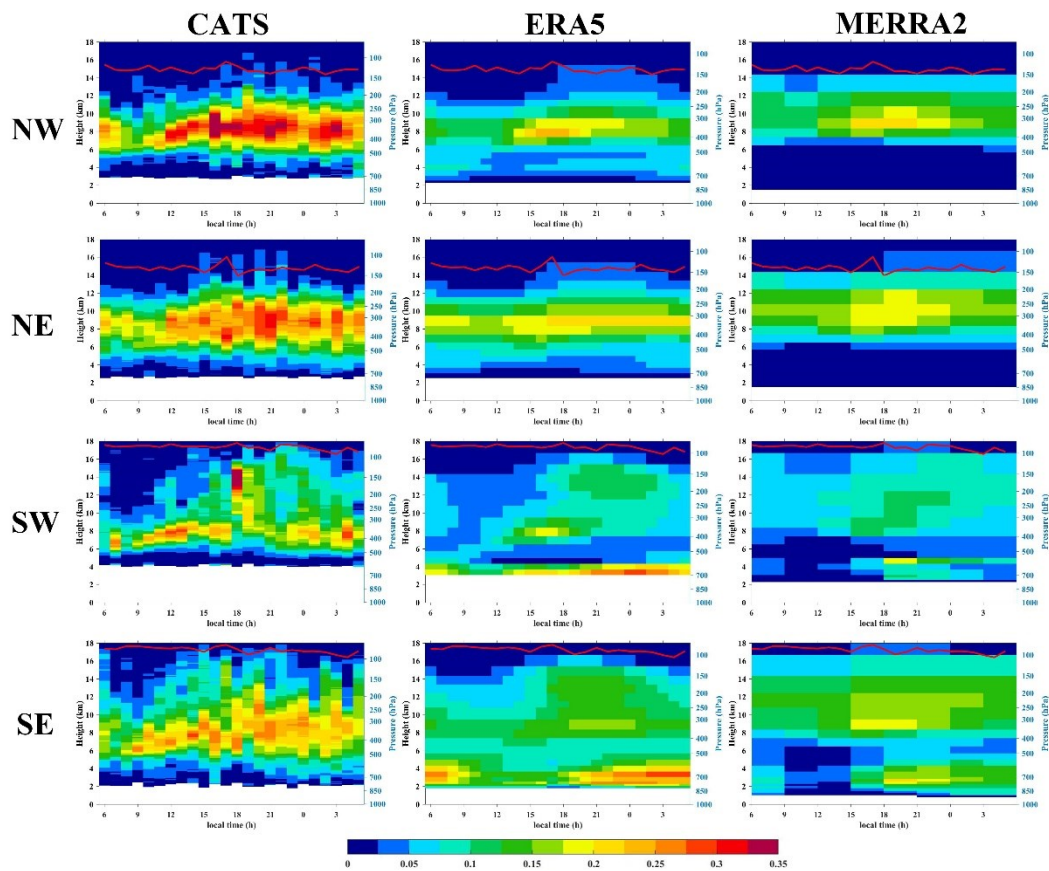




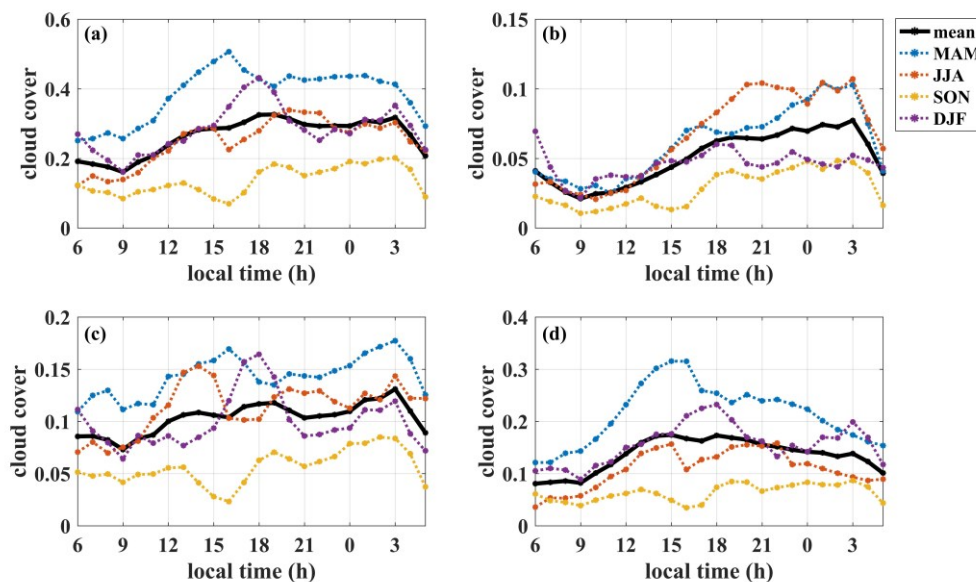
955 **Figure 3: The Taylor diagram describing spatial consistency of total cloud cover between different datasets and CATS every 3 hours. The distance from the origin of the coordinate axis represents the standard deviation for each datasets in spatial distribution. The distance from the red dot labelled ‘CATS’ represents centred root-mean-square deviation (RMSD, purple circle). The time represented by each image is displayed in the upper-right corner, and the time here is local time.**



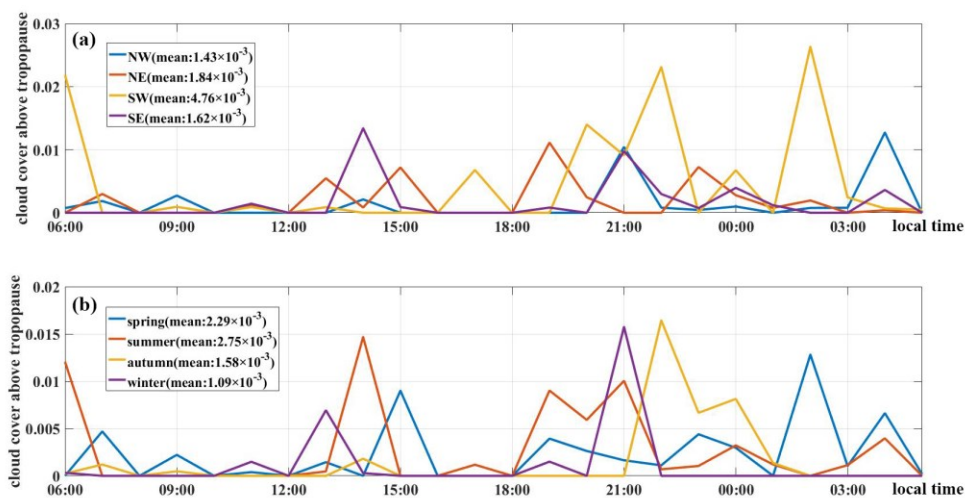
960 **Figure 4: The cloud vertical structure in different regions of TP based on CALIPSO (blue lines), 2B-GEOPROF-lidar (CALIPSO&CloudSat, red lines), CATS (yellow lines), ERA5 (purple lines), MERRA-2 (green lines) at 13:30 LT. (a) The whole TP (b) The northwestern TP (c) The northeastern TP (d) The southwestern TP (e) The southeastern TP. The regions are divided by latitude and longitude lines of 33°N and 89°E (shown in Fig. 1).**



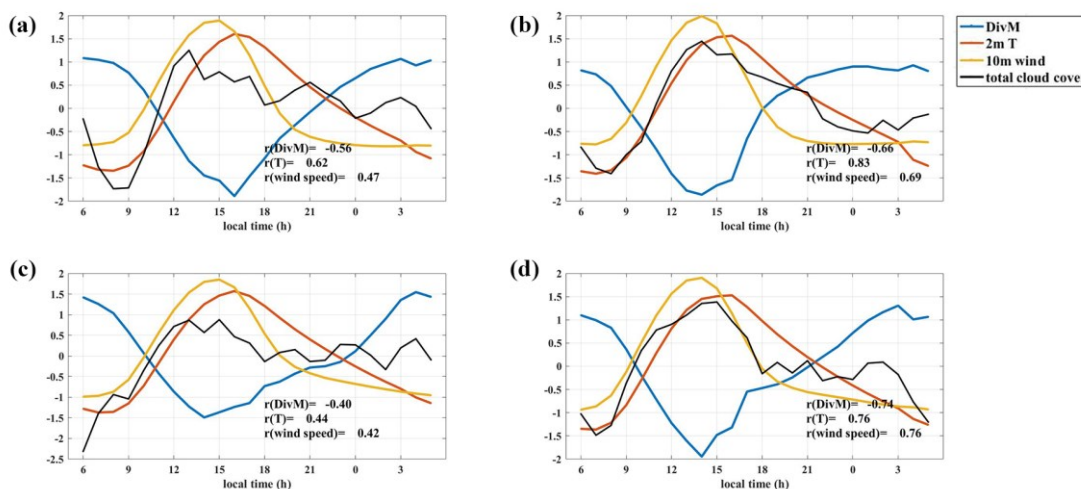
965 **Figure 5:** The hourly vertical distribution of cloud cover over different regions of TP based on CATS, ERA5, MERRA-2. The red lines represent the tropopause height. The first to fourth lines represent the results over the northwestern TP, the northeastern TP, the southwestern TP and the southeastern TP, respectively. The regions are divided by latitude and longitude lines of 33°N and 89°E (shown in Fig. 1).



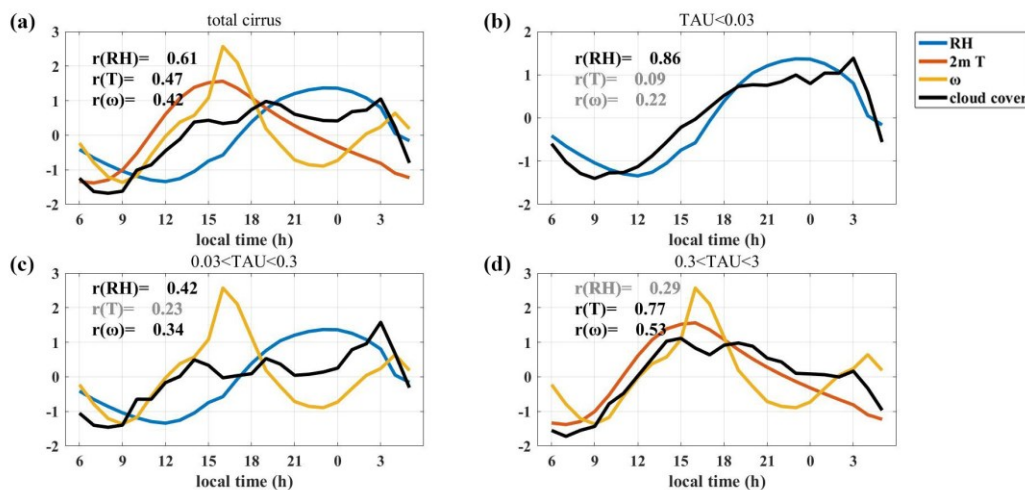
970 **Figure 6:** The hourly cloud cover of different types of cirrus of different seasons. The black lines represent the results of annual average, the blue lines represent the results of spring, the red lines represent the results of summer, the yellow lines represent the results of autumn, the purple lines represent the results of winter. All seasons here are northern hemisphere seasons. (a) represents the cloud cover of all cirrus. (b) represents the subvisible cirrus (optical thickness less than 0.03). (c) represents the thin cirrus (optical thickness between 0.03 and 0.3). (d) represents the opaque cirrus (optical thickness between 0.3 and 3).



975 **Figure 7:** The hourly cloud cover of cirrus shooting over tropopause based on CATS for different regions (a) and different seasons (b). The regions are divided by latitude and longitude lines of 33°N and 89°E (shown in Fig. 1). The average of the whole day of each region is indicated in the legend. All seasons here are northern hemisphere seasons.



980 **Figure 8:** The normalization total cloud cover (black lines) and vertically integrated divergence of moisture flux ($\text{kg/m}^2\text{s}^{-1}$) (blue lines), 2-m temperature (K) (red lines), 10-m wind speed (m/s) (yellow lines) of the different regions of TP. (a) The northwestern TP (b) The northeastern TP (c) The southwestern TP (d) The southeastern TP. Only factors that pass the significance test by 90% are shown as color lines. The correlation coefficients are indicated in the bottom right corner.



985 **Figure 9:** The normalization cloud cover of different types of cirrus (black lines) and 250 hPa relative humidity (%) (blue lines), 2-m temperature (K) (red lines), 250 hPa vertical velocity (Pa/s) (yellow lines) over the TP. (a) all cirrus. (b) the subvisible cirrus (optical thickness less than 0.03). (c) the thin cirrus (optical thickness between 0.03 and 0.3). (d) the opaque cirrus (optical thickness between 0.3 and 3). Only factors that pass the significance test by 90% are shown as color lines. The correlation coefficients are indicated in the upper left corner. The correlation coefficients of the factors that fail the significant test by 90% are colored gray.

990